



Assessment of NO₂ observations during DISCOVER-AQ and KORUS-AQ field campaigns

Sungyeon Choi^{1,2}, Lok N. Lamsal^{1,3}, Melanie Follette-Cook^{1,4}, Joanna Joiner¹, Nikolay A. Krotkov¹, William H. Swartz⁵, Kenneth E. Pickering^{1,6}, Christopher P. Loughner^{6,7}, Wyatt Appel⁸, Gabriele Pfister⁹, Pablo E. Saide¹⁰, Ronald C. Cohen¹¹, Andrew J. Weinheimer⁹, and Jay R. Herman^{1,12}

¹NASA Goddard Space Flight Center, Greenbelt, MD 20771, USA

²Science Systems and Applications, Inc., Lanham, MD 20706, USA

³Universities Space Research Association, Columbia, MD 21046, USA

⁴Morgan State University, Baltimore, MD 20251, USA

⁵Johns Hopkins University, Applied Physics Laboratory, Laurel, MD 20723, USA

⁶University of Maryland, College Park, MD 20742, USA

⁷NOAA Air Resources Laboratory, College Park, MD 20740, USA

⁸Environmental Protection Agency, Research Triangle Park, NC 27709, USA

⁹National Center for Atmospheric Research, Boulder, CO 80301, USA

¹⁰University of California, Los Angeles, CA 90095, USA

¹¹University of California, Berkeley, CA 94720, USA

¹²University of Maryland Baltimore County, Baltimore, MD 21250, USA

Correspondence: Sungyeon Choi (sungyeon.choi@nasa.gov)

Abstract. NASA's Deriving Information on Surface Conditions from Column and Vertically Resolved Observations Relevant to Air Quality (DISCOVER-AQ) campaign in the United States and the joint NASA and National Institute of Environmental Research (NIER) Korea-United States Air Quality Study (KORUS-AQ) in South Korea were two field study programs that provided comprehensive, integrated datasets of airborne and surface observations of atmospheric constituents, including nitrogen dioxide (NO₂), with a goal of improving the interpretation of spaceborne remote sensing data. Various types of NO₂ measurements were made, including in situ concentrations and column amounts of NO₂ using ground- and aircraft-based instruments, while NO₂ column amounts were being derived from the Ozone Monitoring Instrument (OMI) on the Aura satellite. This study takes advantage of these unique data sets by first evaluating in situ data taken from two different instruments on the same aircraft platform, comparing coincidentally sampled profile-integrated columns from aircraft spirals with remotely sensed column observations from ground-based Pandora spectrometers, intercomparing column observations from the ground (Pandora), aircraft (in situ vertical spirals), and space (OMI), and evaluating NO₂ simulations from coarse Global Modeling Initiative (GMI) and high-resolution regional models. We then use these data to interpret observed discrepancies due to differences in sampling and deficiencies in the data reduction process. Finally, we assess satellite retrieval sensitivity to observed and modeled a priori NO₂ profiles. Contemporaneous measurements from two aircraft instruments that likely sample similar air masses generally agree very well but are also found to differ in integrated columns by up to 31.9%. These show even larger differences with Pandora, reaching up to 53.9%, potentially due to a combination of strong gradients in NO₂ fields that could be missed by aircraft spirals and errors in the Pandora retrievals. OMI NO₂ values are about a factor of two lower in these highly polluted



environments, due in part to inaccurate retrieval assumptions (e.g., a priori profiles), but mostly to OMI's areal ($> 312 \text{ km}^2$) averaging.

20 1 Introduction

Nitrogen dioxide (NO_2) plays an important role in the troposphere by altering ozone production and OH radical concentration (Murray et al., 2012, 2014). It is one of the six United States Environmental Protection Agency (EPA) criteria pollutants because of its adverse health effects on humans (WHO, 2013). Major sources of nitrogen oxides ($\text{NO}_x = \text{NO} + \text{NO}_2$) in the troposphere include combustion, soil, and lightning. As a trace gas with a relatively short lifetime, NO_2 is usually confined to
25 a local scale with respect to its source and therefore exhibits strong spatial and temporal variations, leading to difficulties in comparing NO_2 observations by methods with different atmospheric sampling.

Due to its distinct absorption features at ultraviolet/visible (UV/VIS) wavelengths, atmospheric NO_2 is observable from ground- and space-based remote sensing instruments. In particular, space-based measurements of tropospheric column NO_2 have been widely used to study spatial and temporal patterns (e.g., Beirle et al., 2003; Richter et al., 2005; Boersma et al.,
30 2008; Lu and Streets, 2012; Wang et al., 2012; Hilboll et al., 2013; Russell et al., 2010, 2012; Duncan et al., 2013; Lin et al., 2015), and long-term trends (e.g., van der A et al., 2008; Lamsal et al., 2015; Krotkov et al., 2016), and to infer NO_x sources (e.g., Jaeglé et al., 2005; van der A et al., 2008; Bucsela et al., 2010; de Wildt et al., 2012; Lin, 2012; Ghude et al., 2010, 2013a; Mebust and Cohen, 2013; Pickering et al., 2016) and top-down NO_x emissions (e.g., Martin et al., 2003; Konovalov et al., 2006; Zhao and Wang, 2009; Lin et al., 2010; Lamsal et al., 2011; Ghude et al., 2013b; Vinken et al., 2014; Schreier et al., 2015; Cooper et al., 2017; Miyazaki et al., 2017; Liu et al., 2018). These observations have also been often used to assess
35 chemical mechanisms (e.g., Martin et al., 2002; van Noije et al., 2006; Lamsal et al., 2008; Kim et al., 2009; Herron-Thorpe et al., 2010; Huijnen et al., 2010) as well as to infer the lifetime of NO_x (e.g., Schaub et al., 2007; Lamsal et al., 2010; Beirle et al., 2011) in chemical transport models (CTMs). Surface NO_2 concentrations (Lamsal et al., 2008, 2014; Novotny et al., 2011; Bechle et al., 2013) and NO_x deposition flux (Nowlan et al., 2014; Geddes and Martin, 2017) can also be estimated
40 using satellite NO_2 observations. As the accuracy of any applications of satellite data largely depends on the data quality, validation of satellite NO_2 observations is necessary.

A number of validation studies of space-based tropospheric NO_2 columns have been conducted using independent NO_2 observations from airborne in situ mixing ratio measurements (e.g., Boersma et al., 2008; Bucsela et al., 2008; Hains et al., 2010; Lamsal et al., 2014), ground-based total (e.g., Pandora instrument (Herman et al., 2009)) and tropospheric (e.g., MAX-
45 DOAS instrument (e.g., Vlemmix et al., 2010; Irie et al., 2012)) column measurements, and airborne high-resolution DOAS measurements (Lamsal et al., 2017; Nowlan et al., 2018). Most validation studies utilizing in situ/ground-based observations have reported that satellite measurements tend to underestimate tropospheric NO_2 columns, especially over highly polluted areas (e.g., Hains et al., 2010). Intrinsic limits of space-based measurements, however, pose a challenge in comparisons between satellite and in situ/ground-based measurements due to differences in representativeness. As stated above, NO_2 usually exhibits
50 very sharp spatial gradients (tens of meters to kilometers). In contrast, the spatial resolution of satellite measurements is too



coarse (tens of kilometers) to capture the fine spatial features of tropospheric NO₂ abundance. Therefore, it is important to recognize and account for the spatial variability while comparing satellite data with ground-based and in situ observations.

While the intrinsic resolution of satellite observations cannot be altered, there are ways to improve the derived satellite data products. The fidelity of the retrieved NO₂ product is dependent on the assumptions (e.g., NO₂ vertical profile shape, surface reflectivity) made in the retrieval algorithm. Some of the input parameters are available at much coarser resolution than the spatial resolution of OMI, introducing spatially (e.g., rural-to-urban) varying retrieval biases. Several studies show that the use of high-resolution NO₂ profiles results in significant improvements in retrievals (e.g., Russell et al., 2012; Lin et al., 2014; Lamsal et al., 2014; McLinden et al., 2014; Laughner et al., 2016, 2019; Goldberg et al., 2017). Deficiencies in model distributions of NO₂ may be identified and improved through rigorous evaluation with independent data, such as the suite of data collected during the Deriving Information on Surface Conditions from Column and Vertically Resolved Observations Relevant to Air Quality (DISCOVER-AQ) campaign deployments.

In this paper, we use comprehensive, integrated datasets of NO₂ gathered from surface, aircraft, and space instruments during NASA's DISCOVER-AQ and NASA's and NIER's Korea-United States Air Quality Study (KORUS-AQ) together with NO₂ model simulations to address questions regarding retrieval accuracy. We describe the datasets in Section 2.1 and the models in Section 2.2. As an example, we focus on the NASA Standard NO₂ Product from OMI onboard the Aura satellite and conduct retrieval studies using the algorithm as discussed in Section 2.3, but the approaches discussed here could be applied to similar products as well. Results are presented in Section 3.

2 Observations and Chemical Transport Models

2.1 NO₂ observations during DISCOVER-AQ and KORUS-AQ field campaigns

DISCOVER-AQ (<https://www-air.larc.nasa.gov/missions/discover-aq/>) and KORUS-AQ (<https://www-air.larc.nasa.gov/missions/korus-aq/>) were field study programs that provided comprehensive, integrated datasets of airborne and surface observations relevant to the diagnosis of surface air quality conditions from space. DISCOVER-AQ was a part of the NASA Earth Venture program and conducted four field deployments in Maryland (MD), California (CA), Texas (TX), and Colorado (CO) that covered different seasons and pollution regimes. KORUS-AQ was an international cooperation field study program conducted in the Republic of Korea (South Korea), sponsored by NASA and South Korean Government NIER. Table 1 summarizes the campaign locations and periods for the two field campaigns.

The primary objectives of DISCOVER-AQ and KORUS-AQ included (1) exploring the relationship between air quality at the surface and the tropospheric columns that can be derived from satellite orbit, (2) examining the diurnal variation of these relationships, and (3) characterizing the scales of variability relevant to the model simulation and remote observation of air quality. To accomplish these objectives, an observing strategy was designed to carry out systematic and concurrent in situ and remote sensing observations from a network of ground sites and research aircraft. The payloads on research aircraft consisted of several in situ instruments that differed minimally between campaigns. Ground-based trace gas observations included in situ surface and remote sensing Pandora measurements (Herman et al., 2009).



Figure 1 illustrates a conceptual view of the instruments and their sampling methods and areal coverage for NO₂ observations. While the aircraft (P-3B for DISCOVER-AQ and DC-8 for KORUS-AQ) make spirals (P-3B) or ascents/descents (DC-8) over the site, the on-board NCAR and TD-LIF instruments measure in situ NO₂ profiles. The aircraft usually visit each site 2-4 times a day to observe the diurnal variations of the NO₂ profiles. Pandora and NO₂ ground monitor instruments are typically located at ground stations close to the aircraft profiles. Throughout the day, Pandora reports the total column NO₂ from direct-sun measurements and the ground monitor reports the in situ surface NO₂ mixing ratio. Finally, OMI retrievals report a tropospheric column NO₂ once a day in the afternoon; the OMI pixel has a much larger ground footprint as compared with the in situ and Pandora measurements. Table 2 lists the sites with ground-based NO₂ monitors used in this analysis, along with the type of instrument employed at each site and the numbers of aircraft profiles and Pandora measurements available from each site near the time of OMI overpass. Detailed data descriptions follow in this section.

2.1.1 Vertical distribution of NO₂ by aircraft

In situ NO₂ volume mixing ratios (VMRs) were measured from the NASA P-3B (DISCOVER-AQ) and DC-8 (KORUS-AQ) aircraft. The number of flights varied between campaigns, ranging from 10 for Texas to 22 for Korea. Flights took place during a range of conditions, e.g., pollution episodes, clean days, weekdays, and weekends. Measurements usually commenced in the morning and continued throughout the day with multiple sorties on a given day. During each sortie, the aircraft made vertical spirals over surface sites, sampling NO₂ between ~300 m and 5 km from the Earth's surface. In Maryland, spirals were also made over the Chesapeake Bay area, which did not have any ground monitors.

Airborne measurements were carried out using two different instruments and measurement techniques. The four-channel chemiluminescence instrument from the National Center for Atmospheric Research (NCAR) measured NO₂ by photolysis of NO₂ and subsequent chemiluminescence detection of NO₂ following oxidation of the photolysis product NO with ozone (Ridley and Grahek, 1990). This instrument has an NO₂ measurement uncertainty of 10% and a 1-s, 2-sigma detection limit of 50 parts per trillion by volume (pptv). We hereafter refer to these NO₂ measurements as “NCAR”. The thermal dissociation laser-induced fluorescence (TD-LIF) method used by the University of Berkeley detects NO₂ directly and other nitrogen species (e.g., total peroxy nitrates, alkyl nitrates, HNO₃) following thermal dissociation of all oxides of nitrogen (NO_y) to NO₂ (Thornton et al., 2000). The laser-induced fluorescence method is highly sensitive for measuring NO₂, with a detection limit of 30 pptv. The measurement uncertainty is 5%. This instrument has a lower NO₂ sampling frequency than the NCAR instrument due to its alternating measurement cycle for different species. We refer these NO₂ measurements as “TD-LIF”.

Here we use 1-second merged data provided in the campaign data archives, and focus on early afternoon measurements made within 1.5 h of the OMI overpass time (1:30 pm, approximately). Figure 2 shows the mean NO₂ profile for each of the DISCOVER-AQ and KORUS-AQ campaigns. Measurements show considerable spatio-temporal variation as well as some indication of a well-developed mixing layer with the maximum mixing ratio near to the ground. The mixing layer heights vary with region and season. For example, in the MD campaign conducted in summer, the mixing layer stretches up to 800 hPa (2 km). In contrast, the mean profiles from the CA campaign conducted in winter show a shallow mixing layer extending only up to 950 hPa (~700 m). Near-surface NO₂ mixing ratios also vary with the campaign locations and possibly with seasons with



highest near surface NO₂ in CA. In South Korea, the mean near-surface NO₂ mixing ratio is not as high as in CA, but a very high (~5 ppbv) NO₂ mixing ratio stretches up to 850 hPa, resulting in the greatest NO₂ column. While NCAR and TD-LIF mean profiles generally agree with each other in the MD, CA, and CO campaigns, they exhibit larger differences in TX and South Korea.

2.1.2 In situ surface NO₂ measurements

To extend the altitude range of the vertical profiles discussed in Section 2.1.1, we merge in situ aircraft profile measurements with coincident in situ surface NO₂ measurements sampled over the duration of spirals (~20 minutes) by linearly interpolating the NO₂ mixing ratios between the surface and the lowest aircraft altitudes. These new merged profiles contain a greater portion of the tropospheric NO₂ column. During both the DISCOVER-AQ and KORUS-AQ campaigns, in situ surface NO₂ monitors were deployed at several ground sites (Table 2). Measurements were carried out using one of four different types of NO₂ monitors, including chemiluminescence NO_x monitor equipped with either molybdenum or photolytic converter, Cavity Attenuated Phase Shift (CAPS), and Cavity Ring-Down Spectroscopy (CRDS). The molybdenum converter analyzer measures NO₂ indirectly by thermal conversion of NO₂ to NO using molybdenum and detection of NO by chemiluminescence that results from the reaction of NO with ozone. Since the reduction process could convert not only NO₂ but also other reactive nitrogen species, this instrument could overestimate NO₂ concentrations (Dunlea et al., 2007; Steinbacher et al., 2007; Lamsal et al., 2008; Dickerson et al., 2019). The magnitude of interference depends on the relative concentration of NO₂, nitric acid, alkyl nitrates, and peroxy-acetyl nitrate, which vary spatially, diurnally, and seasonally, and is difficult to quantify. Considering their use in the sections below (Sections 2.3.2 and 3), we conducted a sensitivity study examining how 0–50% biases in molybdenum converter measurements could impact tropospheric columns derived from merged (aircraft + surface) profiles. We found that the errors are usually rather small at < 6% for various sites. Therefore, no attempt is made here to correct for the interference in these measurements, although we identify those sites in Table 2 and figures below.

The operating principle of a photolytic converter analyzer is also gas-phase chemiluminescence, but the use of a photolytic converter to reduce NO₂ to NO makes it more specific to NO₂. As a result, this instrument provides nearly interference-free NO₂ measurements, with the exception of HONO (Ryerson et al., 2000). Measurement uncertainties for 1-hour averages are expected to be ~10% (Fehsenfeld et al., 1990).

The CAPS instrument detects NO₂ by measuring absorption around 450 nm. Baseline measurements spanning minutes to hours with a source of NO₂-free air are needed to determine NO₂ amounts. In contrast to the chemiluminescence/molybdenum converter techniques, CAPS directly detects NO₂. Its specificity for NO₂ is affected by potential interference from species like glyoxal, water vapor, and ozone that absorb light within the bandpass of the instrument. The detection limit is <0.1 ppb for a 10-second measurement. NO₂ measurements from CAPS and chemiluminescence NO_x monitors with molybdenum converter are reported to agree to within 2% (Kebabian et al., 2008).

CRDS is a sensitive and compact detector that measures multiple nitrogen species including NO₂. It employs a laser diode at 405 nm for direct detection of NO₂. Interferences arising from absorption by other trace gases, such as ozone and water vapor, are expected to be small. The measurement precision is 20 ppt at a 1-second time resolution and the accuracy is better than 5%,



which is primarily limited by the NO₂ absorption cross-section used in the data reduction process. The total reactive nitrogen (NO_y) measured by CRDS and chemiluminescence NO_x monitor with molybdenum converter is found to agree to within 12% (Wild et al., 2014).

155 2.1.3 Pandora total column NO₂

In addition to in situ measurements, each campaign hosted ground-based networks of Pandora instruments. Pandora is a small, commercially available sun-viewing spectrometer optimized for detection of trace gases, including NO₂. It measures direct solar spectra in the 280-525 nm spectral range with 0.6 nm resolution. A detailed description of the instrument's design, operation, and retrieval method can be found in Herman et al. (2009, 2018). The NO₂ retrieval algorithm includes (1) a direct-
160 sun spectral fitting method similar to traditional Differential Optical Absorption Spectroscopy (DOAS) (Platt, 1994) using one measurement (or an average of several measurements) as a reference spectrum to derive relative NO₂ slant column densities (SCDs), (2) application of the Modified Langley Extrapolation (MLE) to derive total NO₂ SCDs, and (3) conversion of total NO₂ SCDs to vertical column densities (VCDs) using the direct sun air mass factor (AMF) as follows:

$$\text{VCD} = \text{SCD}/\text{AMF} \quad (1)$$

165 The spectral fitting is performed over the 400-440 nm window; it fits NO₂ cross sections at 254.5 K (Vandaele et al., 1998), ozone (Brion et al., 1993) and a 4th order smoothing polynomial, and applies a wavelength shift and a constant offset. In clear-sky conditions, this instrument provides total NO₂ VCD with precision of 2.7×10^{14} molec cm⁻² and an absolute accuracy of 1.3×10^{15} molec cm⁻² (Herman et al., 2018). Potential sources of error in NO₂ retrievals include calibration of raw data, chosen reference spectrum, and the use of a fixed temperature for the NO₂ cross-section. Pandora NO₂ data have been compared with
170 data from direct-sun Multi-Function DOAS (MFDOAS) and Fourier Transform Ultraviolet Spectrometer (UVFTS) (Herman et al., 2009) and have been found to agree within 12%. These data are regularly used to validate satellite NO₂ retrievals (e.g., Lamsal et al., 2014; Tzortziou et al., 2015, 2018; Ialongo et al., 2016).

Here, we use clear-sky quality controlled (root-mean-square (rms) < 0.05 and errors < 0.05 DU) 80-sec total NO₂ column data averaged over the duration of each aircraft spiral. We infer tropospheric column NO₂ by subtracting the OMI stratospheric
175 column from the Pandora total column to compare with tropospheric NO₂ from in situ and OMI observations.

2.2 NO₂ simulations

2.2.1 GMI simulation

The Global Modeling Initiative (GMI) 3-Dimensional chemical transport model (CTM) simulates the troposphere and strato-
180 sphere (Strahan et al., 2013) with a stratosphere-troposphere chemical mechanism (Duncan et al., 2007) updated with the latest chemical rate coefficients (Burkholder et al., 2015) and time-dependent natural and anthropogenic emissions (Strode et al., 2015). Aerosol fields are computed on-line with the Goddard Chemistry Aerosol Radiation and Transport (GOCART) model (Chin et al., 2014, and references therein). Tropospheric processes such as NO_x production by lightning, scavenging,



and wet and dry deposition are also represented in the model. The GMI simulations used in this work were constrained with meteorology from the Modern-Era Retrospective Analysis for Research and Applications, Version 2 (MERRA-2) meteorological fields (Gelaro et al., 2017) at 72 vertical levels from the surface to 0.01 hPa, with a resolution ranging from ~150 m in the boundary layer to ~1 km in the upper troposphere and lower stratosphere, and at a horizontal spatial resolution of 1.25° longitude × 1.0° latitude.

GMI simulations have been evaluated in the troposphere and stratosphere. Strode et al. (2015) showed good agreement with tropospheric O₃ and NO_x trends in the U.S. in a 1990–2013 hindcast simulation. Strahan et al. (2016) demonstrated realistic seasonal and interannual variability of Arctic composition using comparisons to Aura MLS O₃ and N₂O. The simulation of NO₂ in both the troposphere (Lamsal et al., 2014) and stratosphere (Spinei et al., 2014; Marchenko et al., 2015) have been shown to be in good agreement with independent measurements. We sample the model profile at the times and locations of airborne measurements. Figure 2 compares GMI NO₂ profiles with collocated aircraft measurements during the DISCOVER-AQ and KORUS-AQ field campaigns. The GMI simulation generally captures the vertical distribution of NO₂ in the free-troposphere, is somewhat lower in the middle and upper parts of the mixing layer, and exhibits sharper gradients between the boundary layer and surface. Due to the coarse spatial resolution of the GMI model, the surface pressure of the GMI profiles differs from the measurements, especially over complex terrain in CA, CO, and Korea.

2.2.2 NO₂ simulations using regional models

For each DISCOVER-AQ and KORUS-AQ deployment, a high-resolution model simulation was conducted. We use NO₂ profiles from those simulations to examine their effect on retrievals in Section 2.3.2 and to downscale OMI NO₂ retrievals in Section 2.3.3. Below we provide a brief description of each simulation. Information about model options for these simulations can be found in Table A1 in the Appendix. For most of the campaigns, the near-surface NO₂ concentration and the model profile shapes agree in general with the NCAR and TD-LIF profiles. In TX, however, the CMAQ simulation shows lower mixing ratios than observations throughout the mixing layer (Figure 2).

MD: The Weather Research and Forecasting (WRF) model was run (Loughner et al., 2014) from May 24, 2011 through August 1, 2011 at horizontal resolutions of 36, 12, 4, and 1.33 km with 45 vertical levels from the surface to 100 hPa with 16 levels within the lowest 2 km. Meteorological initial and boundary conditions were taken from the 12 km North American Mesoscale (NAM) model. Output from the 4 and 1.33 km WRF simulations were fed into the Community Multiscale Air Quality (CMAQ; Byun and Schere (2005)). Chemical initial and boundary conditions for the 4 km CMAQ run came from a 12 km CMAQ simulation covering the continental US, which was performed for the GEO-CAPE Regional Observing System Simulation Experiment (OSSE). The creation of the emissions used within the CMAQ simulation is described in Loughner et al. (2014) and Anderson et al. (2014). CMAQ was run with reduced mobile emissions by 50% and an increase in the photolysis frequency of NTR based on Anderson et al. (2014).

CA: The coupled WRF-CMAQ modeling system (Wong et al., 2012) was run from January 1, 2013 through February 28, 2013 (2013 DISCOVER-AQ California campaign period) at horizontal resolutions of 4 and 2 km, with 35 vertical levels from the surface to 50 hPa and an average height of the middle of the lowest layer of 20 m. WRF version 3.8 and CMAQ



version 5.2.1 were used in a coupled format, allowing for frequent communication between the meteorological and chemical transport models and indirect effects from aerosol loading on the meteorological calculations in WRF. Meteorological initial and boundary conditions were taken from the 12 km NAM reanalysis product from NOAA. Observation nudging above the planetary boundary layer (PBL) using four-dimensional data assimilation (FDDA) was applied in WRF. Chemical initial and boundary conditions for the 4 km CMAQ simulation came from a 12 km CMAQ simulation covering the continental US, while initial and boundary conditions for the 2 km simulation were obtained from the 4km WRF-CMAQ simulation. Emissions are based on the 2011 U.S. National Emissions Inventory (NEI) with year-specific updates to point and mobile sources, while biogenic emissions were calculated in-line in CMAQ using the Biogenic Emissions Inventory System (BEIS).

TX: To simulate the DISCOVER-AQ Texas campaign, a WRF model simulation was performed from August 18, 2013 through October 1, 2013, covering the entire field deployment in September 2013. The model was run at 36, 12, and 4 km, and 1.33 horizontal resolutions with 45 levels from the surface to 50 hPa. Meteorological initial and boundary conditions were taken from the 12 km North American Mesoscale (NAM) model. Output from the 4 km and 1.33 km simulations were used to run the CMAQ model. Chemical and initial boundary conditions for the outer domain were taken from the Model for Ozone and Related chemical Tracers (MOZART) Chemical Transport Model (CTM). Detailed information about these simulations and the emissions used can be found at http://aqrp.ceer.utexas.edu/projectinfoFY14_15/14-004/14-004%20Final%20Report.pdf.

CO: For the Colorado deployment, WRF was run from July 9, 2014 through August 20, 2014 at spatial resolutions of 12 km (covering the Western US) and 4 km (covering Colorado). The model top was set at 50 hPa, with 37 levels in the vertical. Analysis fields from the European Centre for Medium-Range Weather Forecasts (ECMWF) were used for meteorological initial and boundary conditions. Chemical initial and boundary conditions for the outer domain were taken from Real Time Air Quality Monitoring System (RAQMS) model output. Further information about this simulation can be found at https://www.colorado.gov/airquality/tech_doc_repository.aspx?action=open&file=FRAPPE-NCAR_Final_Report_July2017.pdf.

Korea: Air quality forecasts were performed using the Weather Research and Forecasting model (Skamarock et al., 2008) coupled to Chemistry (WRF-Chem) (Grell et al., 2005) model to support KORUS-AQ flight planning and post-campaign analysis. The modeling domains consist of a regional domain of 20 km resolution covering major sources of transboundary pollutants affecting the Korean Peninsula: anthropogenic pollution from eastern China, dust from inner China and Mongolia, and wild fires from Siberia (Saide et al., 2014). A 4 km resolution domain was nested and covered the Korean Peninsula and surroundings, which encompassed the region where the DC-8 flights were planned and better resolved local sources. Anthropogenic emissions were developed by Konkuk University for KORUS-AQ forecasting and are described in Goldberg et al. (2019).

2.3 OMI NO₂ observations

The Ozone Monitoring Instrument (OMI) aboard the NASA Aura satellite provides measurements of solar backscatter that are used to retrieve total, stratospheric, and tropospheric NO₂ columns with a native ground resolution varying from 13 km×24 km near nadir to 40 km×250 km at swath edges (Levelt et al., 2006, 2018). The Aura satellite was launched on 15 July 2004 into a Sun synchronous polar orbit with a local equator crossing time of 13:45 in the ascending node. OMI is one of the most



stable UV/Vis satellite instruments providing a long-term high-resolution data record with low degradation (Dobber et al., 2008; DeLand and Marchenko, 2013; Schenkeveld et al., 2017). Since the middle of 2007, an anomaly began to appear in OMI radiances in certain rows affecting all Level 2 products (Schenkeveld et al., 2017). This “row anomaly” can be easily identified and the affected rows are discarded.

255 2.3.1 Standard OMI NO₂ product

Here we use the Standard OMI NO₂ product (OMNO2), version 3.1, with updates from version 3.0 (Krotkov et al., 2017). The NO₂ retrieval algorithm uses the differential optical absorption spectroscopy (DOAS) technique. The retrieval method includes (1) determination of NO₂ slant column density (SCD) using a DOAS spectral fit of the NO₂ cross-section from measured reflectance spectra over the 402-465 nm range; (2) calculation of an air mass factor (AMF) that is required to
260 convert SCD into vertical column density (VCD); and (3) a scheme to separate stratospheric and tropospheric VCDs. The AMF calculation is performed by combining NO₂ measurement sensitivity (scattering weights) from the TOMS RADIative transfer model (TOMRAD, Dave (1964)) with the a priori relative vertical distribution (profile shape) of NO₂ taken from the GMI CTM. Computation of scattering weights requires information on viewing and solar geometries, terrain and cloud reflectivities, terrain and cloud pressures, and cloud cover (radiative cloud fraction).

265 The version used here represents a significant advance over previous versions (Bucsela et al., 2006, 2013; Celarier et al., 2008; Lamsal et al., 2014). It includes an improved DOAS algorithm for retrieving slant column densities (SCDs) as discussed in Marchenko et al. (2015). The key features of the algorithm include more accurate wavelength registration between Earth radiance and solar irradiance spectra, iterative accounting of rotational Raman scattering effect, and sequential SCD retrieval of NO₂ and interfering species (water vapor and glyoxal). Solar irradiance reference spectra are monthly average data derived from
270 OMI measurements instead of an OMI composite solar spectrum used in prior versions. Cloud pressure and cloud fraction are taken from an updated version of the OMCLDO2 cloud product that includes updated look-up tables and O₂-O₂ SCD retrieved with a temperature correction (Veefkind et al., 2016). A priori NO₂ profiles are as discussed in Lamsal et al. (2015) and Krotkov et al. (2017) and use 1° latitude × 1.25° longitude GMI model-based monthly a priori NO₂ profiles with year-specific emissions. This retrieval version also uses more accurate information on terrain pressure that is calculated from high resolution Digital
275 Elevation Model (DEM) data at 3 km resolution and GMI terrain pressure.

2.3.2 Re-calculation of OMI NO₂ AMF using alternative NO₂ profiles

NO₂ vertical profiles, especially in the troposphere, vary strongly in both space and time. The simulated NO₂ profiles from a global CTM (GMI) employed in the operational NO₂ retrieval, while offering a good option at a global scale, may not sufficiently capture the distribution of NO₂ at OMI’s ground resolution. Using pre-calculated scattering weights (Sw) made
280 available in the OMNO2 product and alternative information on vertical NO₂ profile shape (Xa), the OMI NO₂ AMF can be readily re-calculated (Lamsal et al., 2014).

$$\text{AMF}_{\text{trop}} = \frac{\sum_{\text{surface}}^{\text{tropopause}} S_w \cdot X_a}{\sum_{\text{surface}}^{\text{tropopause}} X_a}, \quad (2)$$



where the integral from surface to the tropopause yields the tropospheric AMF (AMF_{trop}). Scattering weights vary with viewing/solar geometry, cloud/aerosol conditions, and surface reflectivity, but they are assumed to be independent of the vertical distribution of NO_2 . The typical vertical distribution of scattering weights is characterized by lower values in the troposphere due to reduced sensitivity owing to Rayleigh scattering and higher values (corresponding to a nearly geometric AMF) in the stratosphere. The AMF is therefore highly sensitive to NO_2 profile shape in the lower troposphere.

Here, we investigate how a priori NO_2 profiles affect OMI tropospheric AMF and consequently the retrieval of OMI tropospheric NO_2 VCD. For this, we combine the measured profile (from surface to ~ 5 km) with coincidentally sampled simulated NO_2 from GMI (5 km to tropopause) to create a complete tropospheric NO_2 profile. We choose the GMI simulation over the high resolution model simulations because we found that the GMI generally better performed in the free-troposphere as compared to the regional models. We then interpolate the pressure-tagged NO_2 observations (aircraft NCAR NO_2 + surface) onto the pressure grid of the OMI NO_2 scattering weight. The tropospheric AMFs obtained using individual measured profiles (AMF_{obs}) are compared with the AMFs in the OMI standard product (AMF_{SP}), which are calculated using the GMI yearly varying monthly climatology (Figure 3a). AMF_{SP} is generally higher than AMF_{obs} by 34% on average, with the largest difference (61.6%) for TX and the smallest difference (16.6%) for Korea; this means that the OMI SP VCDs, based on the AMF_{SP} , are corresponding smaller on average than the those based on measured profiles. The correlation ranges from fair ($r = 0.41$, $N = 21$) for MD and TX to excellent ($r \geq 0.92$, $N = 36$) for CA and Korea.

To explore how NO_2 profiles from high-resolution model simulations could affect OMI NO_2 retrievals, we calculate tropospheric AMFs using simulated monthly NO_2 profiles (AMF_{HR}). Since the OMI ground pixel size is much larger than the model grid boxes, we derive an average profile of all model grid boxes located within one OMI pixel and use it to calculate AMF_{HR} . Figure 3(b) compares AMF_{obs} with AMF_{HR} ; it suggests improved agreement as compared to AMF_{SP} (Figure 3a) especially for CA, CO, and Korea, albeit with no significant improvement in the correlation.

We also considered how using AMFs based on monthly mean profiles, such as the OMI SP, impacts retrieved NO_2 . To assess this, we calculated AMFs using both daily (AMF_{obs}) and campaign-average measured NO_2 profiles (AMF_{obs-m}). Figure 3(c) shows that AMF_{obs} and AMF_{obs-m} agree to within 5.3% and exhibit excellent correlation ($r > 0.8$). That is, the use of a mean profile does not make a significant difference compared to the individual daily profiles, implying that the average profile generally captures the local vertical distribution fairly well. Somewhat larger scatter in TX may be related to stronger land-sea breeze dynamics that could affect the vertical distribution of NO_2 in both the boundary layer and free-troposphere. Our results here differ with previous studies that reported improved agreement of OMI NO_2 retrievals using simulated daily NO_2 profiles with independent observations (Valin et al., 2013; Laughner et al., 2019), although Laughner et al. (2019) also suggested poorer performance with daily profiles in the southeast US than in other regions.

2.3.3 Downscaled OMI NO_2 data

The NO_2 value associated with an OMI ground pixel is averaged over a large area. This spatial smoothing leads to a loss of information on sub-pixel variation, which could be considerable for NO_2 especially over urban source regions. Therefore, it



is important to recognize and address this limitation while assessing, interpreting, and using satellite NO₂ data. Here we use high-resolution NO₂ model simulations for sub-pixel variation.

We apply the method described by Kim et al. (2016, 2018) to downscale OMI NO₂ retrievals, which are then compared with aircraft and Pandora data. This method applies high resolution model-derived spatial-weighting kernels to individual
320 OMI pixels and calculates sub-pixel variability within the pixel. The major assumption is that the model captures the spatial distribution of emission sources and NO₂ transport patterns well. The method ensures that the quantity (total number of molecules) of the satellite data over the pixel is numerically preserved, while adding higher resolution spatial information to the derived tropospheric NO₂ columns.

Figure 4 illustrates the downscaling of tropospheric NO₂ for an OMI pixel using the high resolution CMAQ simulation over
325 Essex, Maryland. The tropospheric NO₂ column observed by OMI (5.9×10^{15} molec cm⁻²) is 25.7% higher than the average of the CMAQ NO₂ columns over the pixel. The spatial weighting kernels suggest more than an order of magnitude difference in NO₂ within this single OMI pixel. Applying the kernels to the original OMI pixel value results in a range of sub-pixel NO₂ column values from 1.9×10^{15} molec cm⁻² over a clean background to 3.2×10^{16} molec cm⁻² over a polluted hotspot.

Figure 5 demonstrates how the downscaled OMI NO₂ data using high-resolution NO₂ output from a CMAQ simulation
330 compares with the original OMI NO₂ data from the standard product. Both OMI SP and CMAQ show enhanced NO₂ columns at major urban areas, but their magnitudes differ, with OMI showing lower values. As described above, OMI's field of view covers a large area, sampling the NO₂ field over the entire pixel, while the actual NO₂ distribution (better resolved by the CMAQ simulation) is defined by local source strengths, chemistry, and wind patterns that can occur at much finer spatial scales. By employing the relative ratios inside an OMI pixel rather than the overall magnitude of simulated columns, the
335 downscaling technique yields a more detailed structure, enhancing NO₂ over sources and dampening elsewhere by more than a factor of two.

3 Results and Discussion

3.1 Comparison between in situ observations

Figure 6a and Table 3 summarize how the two airborne in situ NO₂ tropospheric column measurements compare. We derive the
340 column amount by first extending the NCAR and TD-LIF NO₂ profiles to the same surface NO₂ concentration measurements and then integrating the NO₂ profiles. The only exception is at the Chesapeake Bay of the MD campaign, the only marine site used in this study; we extend a constant NO₂ mixing ratio measured at the lowest aircraft altitudes to the surface. To compare with OMI and Pandora retrievals, NO₂ amounts for the missing portion from the top of aircraft altitude to the tropopause are added from the GMI simulation. This amount varied between 4.7×10^{14} molec cm⁻² and 1.2×10^{15} molec cm⁻² and
345 represented an average 5% of the tropospheric NO₂ columns but can reach up to 50.8% for an individual profile. Overall, the two airborne in situ columns generally agree very well and exhibit excellent correlation ($r = 0.87-0.99$). The correlation and mean difference differ among the five campaigns, with TD-LIF higher than NCAR by 31.9% in TX and 11.6% in Korea but lower by ~10% in MD and CO. The observed difference in TX is much larger than the reported uncertainty of both NCAR and



TD-LIF measurements. Analysis of individual profiles suggests that the data from TD-LIF are generally higher than NCAR at
350 all altitudes, regardless of the NO₂ pollution level (Figure 7). The underlying cause of this difference is not clear, but it may be
associated with the applied calibration standard or an interference issue for either or both of the two measurements. The small
difference elsewhere could come from the lower measurement frequency of TD-LIF as compared with the NCAR instrument.

3.2 Comparison between Pandora and aircraft observations

Figures 6b-6c and Table 3 show the comparison between the Pandora and the two airborne tropospheric NO₂ column mea-
355 surements. We derive tropospheric columns from Pandora by subtracting collocated OMI stratospheric NO₂ columns from the
Pandora total NO₂ column retrievals. The relationship between the aircraft and Pandora data is not as good as between the two
aircraft measurements themselves. The correlation ranges from fair ($r = 0.42$) to excellent ($r = 0.95$) for NCAR versus Pandora
and poor ($r = 0.18$) to excellent ($r = 0.94$) for TD-LIF versus Pandora, with higher correlation in CO, TX, and Korea and
lower correlation in MD and CA. Pandora data are about a factor of two lower than aircraft measurements in TX. Elsewhere,
360 Pandora data agree with aircraft measurements to within 20% on average, although much larger differences are observed for
individual sites. A larger discrepancy for Pandora data in TX is also reported by Nowlan et al. (2018), who used various NO₂
measurements to evaluate Geo-TASO NO₂ retrievals. Reasons for such exceptionally large differences could include strong
gradients in the NO₂ field that are missed by aircraft spirals, errors in Pandora retrievals, or both.

3.3 Assessment of OMI NO₂ retrievals

365 We compare OMI tropospheric NO₂ columns with Pandora data and vertically integrated columns from aircraft spiral at 23
locations (Table 2) during the DISCOVER-AQ and KORUS-AQ field campaigns. Collocated aircraft and Pandora data are
temporally matched to OMI by allowing only the measurements made within 1.5 h of the OMI overpass time. We infer
tropospheric columns from Pandora by subtracting OMI-derived stratospheric NO₂ from Pandora total columns. For OMI, we
include quality-controlled, cloud-free (cloud radiance fraction < 0.5) data from all cross-track positions, but exclude the data
370 affected by the row anomaly.

Figure 8 (a and b) and Table A2 present tropospheric NO₂ columns from the OMI standard product compared with integrated
columns from NCAR and TD-LIF instruments. Although the OMI and aircraft data are significantly correlated ($r = 0.39$ – 0.87),
OMI NO₂ retrievals are generally lower, with largest difference in CO and smallest difference in MD. OMI data are also
lower than Pandora as shown in Figure 8c. The magnitude of the difference and the degree of correlation with OMI vary
375 for NCAR, TD-LIF, and Pandora measurements. This discrepancy between OMI, aircraft spiral columns, and Pandora's local
measurements is due to a combination of strong NO₂ spatial variation, size of OMI pixels, and the placement of the sites, but
OMI retrieval errors arising from inaccurate information in the AMF calculation, such as a priori NO₂ profiles, and potential
errors in the validation sources themselves also contribute.

Figure 8(d-f) and Table A3 show the comparison after partially accounting for OMI retrieval errors arising from a priori
380 NO₂ profiles taken from the GMI model. Replacing the model profiles with the NCAR and TD-LIF observed NO₂ profiles in
the AMF calculations addresses the issues related to model inaccuracies, although the measured profiles may not necessarily



represent the true average NO₂ over the entire OMI pixel (e.g., Figure 4). Nevertheless, using observed profiles reduces OMI's mean differences with NCAR by 8%–29.2%, TD-LIF by 8.7%–24.4%, and Pandora by 6.8%–24.2%. Changes are largest in TX and smallest in CA and Korea. Correlations are either improved or remain similar.

385 Figure 8(g-i) and Table A4 show the comparison of OMI NO₂ columns derived using observed profiles with NCAR, TD-LIF, and Pandora observations after accounting for spatial variation in the NO₂ field as suggested by the CMAQ simulation. After downscaling, agreement of OMI NO₂ columns improves further with NCAR by 1.1%–41.5%, TD-LIF by 1.2%–39.7%, and Pandora by 1.2%–33.2%. Exceptions are MD for both aircraft and Pandora data, and TX for Pandora data only. Changes are small in MD and Korea and large in CA and TX. The larger difference in TX is due to significant underestimation of NO₂
390 by Pandora instruments. The correlation improves in MD and TX, but reduces in CA, CO, and Korea. These results suggest that downscaling helps explain some of the discrepancies between OMI, aircraft, and Pandora observations. Variations among campaign locations may also point to difficulty related to the fidelity of the CMAQ simulations.

Figure 9 summarizes the comparison of OMI with aircraft and Pandora measurements. Here we present site mean columns observed from all measurements during the entire campaign periods. OMI captures the overall spatial variation in site means.
395 In relatively cleaner places (NO₂ VCD $\leq 5 \times 10^{15}$ molec cm⁻²), OMI agrees well with NCAR and TD-LIF columns. OMI values are generally lower in polluted areas.

3.4 Implications for satellite NO₂ validations

NO₂ measurements from a variety of instruments and techniques conducted during the DISCOVER-AQ and KORUS-AQ field deployments provided a unique opportunity to assess correlative data and realize the strengths and limitations of the various
400 measurements. Some of the techniques are still in a state of development and evaluation, and the data have not been fully validated. Additional complications arise when comparing measurements covering different areal extent. This is particularly true for a short-lived trace gas like NO₂ that has a large spatial gradient, especially in the boundary layer.

The NCAR and TD-LIF instruments on board the same aircraft (P-3B during DISCOVER-AQ and DC-8 during KORUS-AQ) offer valuable insights on vertical distribution of NO₂, a critical piece of information needed for satellite retrievals. Despite
405 their adjacent locations on the aircraft, they did not sample the same air mass throughout each profile due to their different NO₂ measurement frequencies. Despite this, and even using independent measurement techniques with unique sources of uncertainties, NO₂ measurements from the two instruments exhibit excellent correlation and very good agreement in most cases. However, varying discrepancies between the two instruments among campaigns with campaign-average differences reaching up to 31.9% is unlikely to be related solely to the sampling issues, but rather to issues pertaining to measurement
410 methods. It is crucial to reconcile these differences and improve the accuracy of these measurements for meaningful validation and improved error characterization of satellite NO₂ retrievals.

In situ aircraft spirals miss significant portions of the tropospheric NO₂ column, especially from the ground to the lowest level of aircraft altitude, typically 200-300 m above ground level. In this analysis, we account for the missing portion above the aircraft profile by using coincidentally sampled simulated NO₂ profiles. For the portion below the aircraft profile we ex-
415 trapolate to surface monitor data. The latter step can be a significant error source, given that it assumes spatial homogeneity



over the spiral domain. Additional errors could come from the use of different types of monitors that were deployed during the DISCOVER-AQ and KORUS-AQ campaigns (see Section 2.1.2). In particular, NO₂ data from molybdenum converter analyzers are biased high by variable amounts that are difficult to quantify and correct (e.g., Lamsal et al., 2008). Use of more accurate NO₂ monitors, such as photolytic converter analyzers, together with balloon-borne NO₂ sondes (Sluis et al., 2010) of
420 similar accuracy would complement in situ aircraft profiles.

While total column NO₂ retrievals from the ground-based remote sensing Pandora instrument are useful to track temporal changes, their use for satellite validation or for comparing with aircraft spiral data can be onerous particularly over locations with large NO₂ spatial gradients, such as cities. Pandora's field of view is so narrow that it serves as a point measurement. Additionally, Pandora data are subject to retrieval errors arising predominantly from the use of an incorrect reference spectrum
425 as well as fixed temperature for the NO₂ cross-section in the spectral fitting procedure. Failure to apply a reference spectrum derived using weeks of measurements from the same site often yields systematic biases in the retrieved NO₂ columns. Improved calibration and data processing are therefore needed to improve the Pandora data quality. Concurrent spatial NO₂ observations from other ground-based (e.g., Multi Axis Differential Optical Absorption Spectroscopy (MAX-DOAS), Vlemmix et al., 2010) or airborne (e.g., Geostationary Trace gas and Aerosol Sensor Optimization (GeoTASO), Nowlan et al., 2016) platforms would
430 facilitate inter-comparison among measurements of different spatial scales.

Validation of NO₂ observations any satellite instrument, including OMI, is complicated by a variety of factors, principally the ground area covered by the instrument's field of view. As discussed in Section 3.3, disagreement between partially (spatially and temporally) matched OMI NO₂ and validation measurements made near sources may be reasonably anticipated, and ought to be expected. Therefore, it may be necessary to use a proper validation strategy, such as downscaling of satellite data using
435 either observed or modeled NO₂ as presented in Figure 8(g-i) and Table A4. It also underscores the need of comprehensive high quality long-term observations for validation. Enhanced agreement with OMI retrievals revised using observed NO₂ profiles is indicative of retrieval errors from model-based a priori vertical NO₂ profile shapes (Figure 8(d-f), Table A3), and highlights the need of approaches to address the issue. Moreover, improved accuracy in other retrieval parameters, both surface and atmospheric, help enhance the quality of satellite NO₂ retrievals (Laughner et al., 2019; Vasilkov et al., 2017, 2018; Lorente
440 et al., 2018; Lin et al., 2014, 2015; Liu et al., 2019; Noguchi et al., 2014; Zhou et al., 2011)

4 Conclusions

We conducted a comprehensive inter-comparison among various NO₂ measurements made during the five field deployments of DISCOVER-AQ and KORUS-AQ. The field campaigns were conducted in four US states (Maryland, California, Texas, and Colorado), and South Korea. The analyzed data sets were obtained from surface monitors, the NCAR and TD-LIF airborne
445 instruments, ground-based Pandora instruments, and space-based OMI. We investigated the data from 23 sites among the 5 campaigns, when measurements from all these instruments were available. We focused on analysis of tropospheric NO₂ column amounts. NO₂ mixing ratio measurements from the surface monitors and airborne instruments were merged and integrated



to yield tropospheric columns while the Pandora tropospheric columns were obtained by subtracting the OMI stratospheric column from Pandora total column observations.

450 In order to compare OMI NO₂ tropospheric columns with the available validation measurements, we used a combination of observed and simulated NO₂ vertical profiles to re-calculate tropospheric NO₂ columns using the OMI Standard Product (OMNO2), version 3.1. To overcome the challenge of comparing OMI NO₂ with its relatively large pixel size to the airborne/ground-based measurements with small spatial scales, we additionally applied a downscaling technique, whereby OMI tropospheric NO₂ columns for each ground pixels are downscaled using high resolution CMAQ (DISCOVER-AQ) or
455 WRF-Chem (KORUS-AQ) model simulations. Therefore, the comparisons here include three kinds of OMI NO₂ tropospheric columns: (1) OMI Standard Product, (2) OMI data re-calculated using observed NO₂ profiles, and (3) downscaled OMI NO₂ data.

The tropospheric columns from the NCAR and TD-LIF airborne instruments generally show good agreement with a mean difference of 8.4% and correlation coefficients in the 0.87–0.99 range. The Pandora columns also agree variably with the two
460 airborne instruments, with the campaign average difference in the range of 3% to 54%, but the correlation is not as good ($r = 0.18–0.95$) as between the two airborne instruments themselves. There are differences among the campaigns. In particular, all three instruments show the largest discrepancies in the TX campaign; TD-LIF is higher than NCAR by ~31.9%, and Pandora data are lower by ~39% and ~54% as compared to NCAR and TD-LIF measurements, respectively.

All three OMI NO₂ columns (Standard Product, based on observed NO₂ profiles, and downscaled) exhibit good correlation with the airborne/ground-based measurements. In terms of quantitative agreement, the OMI SP column is smaller than
465 airborne/ground-based measurements. Retrievals using observed NO₂ profiles bring the OMI column closer to validation measurements. Applying downscaling to OMI data provides further improvement in agreement, albeit little or insignificant change in correlation perhaps due to the use of model simulations for downscaling.

As discussed in section 3.3, disagreement between the comparatively large OMI pixel and smaller scale ground and aircraft
470 measurements is to be expected due to the large spatial variability of NO₂. Techniques such as the downscaling method shown here can reduce this discrepancy. However, robust evaluation of NO₂ tropospheric column retrievals is further confounded by the current lack of agreement among ground based and in-situ measurements. Future validation strategies for satellite observations of tropospheric column NO₂ will need to address these differences.

Data availability. Airborne and ground-based, and Pandora NO₂ data during the DISCOVER-AQ and KORUS-AQ campaigns are available
475 at the NASA Langley's campaign data web archive (<https://www-air.larc.nasa.gov/index.html>). OMI NO₂ Standard Product (SP) data are available at NASA Goddard Earth Sciences Data and Information Services Center (GES DISC) (<https://disc.gsfc.nasa.gov>).

Appendix A

This section includes Table A1–A4.



480 *Author contributions.* SC, LL, JJ, NAK, MFC, WHS, and KEP designed the data analysis. CPL, WA, GP, and PES provided the model simulations. RCC and AJW provided the airborne in situ measurements. JRH provided the ground-based Pandora measurements. SC, LL, MFC, WHS, CPL, WA and PS wrote the manuscript with comments from all coauthors.

Competing interests. The authors declare that no competing interests are present.

485 *Acknowledgements.* The work was supported by NASA's EarthScience Division through an Aura Science team and Atmospheric Composition Modeling and Analysis Program (ACMAP) grants. The Dutch–Finnish-built OMI instrument is part of the NASA EOSAura satellite payload. The OMI instrument is managed by KNMI and the Netherlands Agency for Aero-space Programs (NIVR). P. E. Saide would like to acknowledge support from NASA grant NNX11AI52G. Authors thank all principal investigators and their staffs for providing ground- and aircraft-based NO₂ measurements during the DISCOVER-AQ and KORUS-AQ campaigns.



References

- Anderson, D. C., Loughner, C. P., Diskin, G., Weinheimer, A., Canty, T. P., Salawitch, R. J., Worden, H. M., Fried, A., Mikoviny, T.,
490 Wisthaler, A., and Dickerson, R. R.: Measured and modeled CO and NO_y in DISCOVER-AQ: An evaluation of emissions and chemistry
over the eastern US, *Atmospheric Environment*, 96, 78–87, <https://doi.org/10.1016/j.atmosenv.2014.07.004>, <http://www.sciencedirect.com/science/article/pii/S1352231014005251>, 2014.
- Bechle, M. J., Millet, D. B., and Marshall, J. D.: Remote sensing of exposure to NO₂: Satellite versus ground-based measurement in a large
495 urban area, *Atmos. Environ.*, 69, 345–353, <https://doi.org/10.1016/j.atmosenv.2012.11.046>, <http://www.sciencedirect.com/science/article/pii/S1352231012011144>, 2013.
- Beirle, S., Platt, U., Wenig, M., and Wagner, T.: Weekly cycle of NO₂ by GOME measurements: a signature of anthropogenic sources,
Atmos. Chem. Phys., 3, 2225–2232, <https://doi.org/https://doi.org/10.5194/acp-3-2225-2003>, <https://www.atmos-chem-phys.net/3/2225/2003/>, 2003.
- Beirle, S., Boersma, K. F., Platt, U., Lawrence, M. G., and Wagner, T.: Megacity emissions and lifetimes of nitrogen oxides probed from
500 space, *Science*, 333, 1737–1739, <https://doi.org/10.1126/science.1207824>, <https://science.sciencemag.org/content/333/6050/1737>, 2011.
- Boersma, K. F., Jacob, D. J., Bucsela, E. J., Perring, A. E., Dirksen, R., van der A, R. J., Yantosca, R. M., Park, R. J., Wenig, M. O.,
Bertram, T. H., and Cohen, R. C.: Validation of OMI tropospheric NO₂ Observations During INTEX-B and application to constrain NO_x
emissions over the eastern United States and Mexico, *Atmos. Environ.*, 42, 4480–4497, <https://doi.org/10.1016/j.atmosenv.2008.02.004>,
<https://dash.harvard.edu/handle/1/3579187>, 2008.
- 505 Brion, J., Chakir, A., Daumont, D., Malicet, J., and Parisse, C.: High-resolution laboratory absorption cross section of O₃. Temperature
effect, *Chem. Phys. Lett.*, 213, 610–612, [https://doi.org/10.1016/0009-2614\(93\)89169-I](https://doi.org/10.1016/0009-2614(93)89169-I), <http://www.sciencedirect.com/science/article/pii/000926149389169I>, 1993.
- Bucsela, E. J., Celarier, E. A., Wenig, M. O., Gleason, J. F., Veefkind, J. P., Boersma, K. F., and Brinksma, E. J.: Algorithm
for NO₂ vertical column retrieval from the ozone monitoring instrument, *IEEE Trans. Geosci. Remote Sens.*, 44, 1245–1258,
510 <https://doi.org/10.1109/TGRS.2005.863715>, 2006.
- Bucsela, E. J., Perring, A. E., Cohen, R. C., Boersma, K. F., Celarier, E. A., Gleason, J. F., Wenig, M. O., Bertram, T. H., Wooldridge,
P. J., Dirksen, R., and Veefkind, J. P.: Comparison of tropospheric NO₂ from in situ aircraft measurements with near-real-time and
standard product data from OMI, *Journal of Geophysical Research: Atmospheres*, 113, <https://doi.org/10.1029/2007JD008838>, <https://agupubs.onlinelibrary.wiley.com/doi/abs/10.1029/2007JD008838>, 2008.
- 515 Bucsela, E. J., Pickering, K. E., Huntemann, T. L., Cohen, R. C., Perring, A., Gleason, J. F., Blakeslee, R. J., Albrecht, R. I., Holzworth, R.,
Cipriani, J. P., Vargas-Navarro, D., Mora-Segura, I., Pacheco-Hernández, A., and Laporte-Molina, S.: Lightning-generated NO_x seen by
the Ozone Monitoring Instrument during NASA's Tropical Composition, Cloud and Climate Coupling Experiment (TC4), *J. Geophys. Res.*
Atmos., 115, D00J10, <https://doi.org/10.1029/2009JD013118>, <https://agupubs.onlinelibrary.wiley.com/doi/abs/10.1029/2009JD013118>,
2010.
- 520 Bucsela, E. J., Krotkov, N. A., Celarier, E. A., Lamsal, L. N., Swartz, W. H., Bhartia, P. K., Boersma, K. F., Veefkind, J. P., Gleason, J. F.,
and Pickering, K. E.: A new stratospheric and tropospheric NO₂ retrieval algorithm for nadir-viewing satellite instruments: applications
to OMI, *Atmos. Meas. Tech.*, 6, 2607–2626, <https://doi.org/https://doi.org/10.5194/amt-6-2607-2013>, <https://www.atmos-meas-tech.net/6/2607/2013/amt-6-2607-2013.html>, 2013.



- Burkholder, J., Sander, S., Abbatt, J., Barker, J., Huie, R., Kolb, C., Kurylo, M., Orkin, V., Wilmouth, D., and Wine, P.: Chemical Kinetics and Photochemical Data for Use in Atmospheric Studies: Evaluation Number 18, Tech. rep., JPL Publication 15-10, Pasadena, California, USA, 2015.
- Byun, D. and Schere, K.: Review of the Governing Equations, Computational Algorithms and Other Components of the Models-3 Community Multiscale Air Quality (CMAQ) Modeling System, *Appl. Mech. Rev.*, 59, 51–78, 2005.
- Celarié, E. A., Brinkma, E. J., Gleason, J. F., Veeffkind, J. P., Cede, A., Herman, J. R., Ionov, D., Goutail, F., Pommereau, J.-P., Lambert, J.-C., Roozendael, M. v., Pinardi, G., Wittrock, F., Schönhardt, A., Richter, A., Ibrahim, O. W., Wagner, T., Bojkov, B., Mount, G., Spinei, E., Chen, C. M., Pongetti, T. J., Sander, S. P., Bucselá, E. J., Wenig, M. O., Swart, D. P. J., Volten, H., Kroon, M., and Levelt, P. F.: Validation of Ozone Monitoring Instrument nitrogen dioxide columns, *J. Geophys. Res. Atmos.*, 113, D15S15, <https://doi.org/10.1029/2007JD008908>, <https://agupubs.onlinelibrary.wiley.com/doi/abs/10.1029/2007JD008908>, 4010.1002/%28ISSN%292169-8996.AURA1, 2008.
- Chin, M., Diehl, T., Tan, Q., Prospero, J. M., Kahn, R. A., Remer, L. A., Yu, H., Sayer, A. M., Bian, H., Geogdzhayev, I. V., Holben, B. N., Howell, S. G., Huebert, B. J., Hsu, N. C., Kim, D., Kucsera, T. L., Levy, R. C., Mishchenko, M. I., Pan, X., Quinn, P. K., Schuster, G. L., Streets, D. G., Strode, S. A., Torres, O., and Zhao, X.-P.: Multi-decadal aerosol variations from 1980 to 2009: a perspective from observations and a global model, *Atmos. Chem. Phys.*, 14, 3657–3690, <https://doi.org/https://doi.org/10.5194/acp-14-3657-2014>, <https://www.atmos-chem-phys.net/14/3657/2014/acp-14-3657-2014.html>, 2014.
- Cooper, M., Martin, R. V., Padmanabhan, A., and Henze, D. K.: Comparing mass balance and adjoint methods for inverse modeling of nitrogen dioxide columns for global nitrogen oxide emissions, *J. Geophys. Res. Atmos.*, 122, 4718–4734, <https://doi.org/10.1002/2016JD025985>, <https://agupubs.onlinelibrary.wiley.com/doi/abs/10.1002/2016JD025985>, 2017.
- Dave, J. V.: Importance of higher order scattering in a molecular atmosphere, *J. Opt. Soc. Am.*, *JOSA*, 54, 307–315, <https://doi.org/10.1364/JOSA.54.000307>, <https://www.osapublishing.org/josa/abstract.cfm?uri=josa-54-3-307>, 1964.
- de Wildt, M. d. R., Eskes, H., and Boersma, K. F.: The global economic cycle and satellite-derived NO₂ trends over shipping lanes, *Geophys. Res. Lett.*, 39, L01 802, <https://doi.org/10.1029/2011GL049541>, <https://agupubs.onlinelibrary.wiley.com/doi/abs/10.1029/2011GL049541>, 2012.
- DeLand, M. and Marchenko, S.: The solar chromospheric Ca and Mg indices from Aura OMI, *J. Geophys. Res. Atmos.*, 118, 3415–3423, <https://doi.org/10.1002/jgrd.50310>, <https://agupubs.onlinelibrary.wiley.com/doi/abs/10.1002/jgrd.50310>, 2013.
- Dickerson, R. R., Anderson, D. C., and Ren, X.: On the use of data from commercial NO_x analyzers for air pollution studies, *Atmos. Environ.*, 214, 116 873, <https://doi.org/10.1016/j.atmosenv.2019.116873>, <http://www.sciencedirect.com/science/article/pii/S1352231019305035>, 2019.
- Dobber, M., Kleipool, Q., Dirksen, R., Levelt, P., Jaross, G., Taylor, S., Kelly, T., Flynn, L., Leppelmeier, G., and Rozemeijer, N.: Validation of Ozone Monitoring Instrument level 1b data products, *J. Geophys. Res. Atmos.*, 113, D15S06, <https://doi.org/10.1029/2007JD008665>, <https://agupubs.onlinelibrary.wiley.com/doi/abs/10.1029/2007JD008665>, 2008.
- Duncan, B. N., Strahan, S. E., Yoshida, Y., Steenrod, S. D., and Livesey, N.: Model study of the cross-tropopause transport of biomass burning pollution, *Atmos. Chem. Phys.*, 7, 3713–3736, <https://doi.org/https://doi.org/10.5194/acp-7-3713-2007>, <https://www.atmos-chem-phys.net/7/3713/2007/>, 2007.
- Duncan, B. N., Yoshida, Y., de Foy, B., Lamsal, L. N., Streets, D. G., Lu, Z., Pickering, K. E., and Krotkov, N. A.: The observed response of Ozone Monitoring Instrument (OMI) NO₂ columns to NO_x emission controls on power plants in the United States: 2005–2011, *Atmos. Environ.*, 81, 102–111, <https://doi.org/10.1016/j.atmosenv.2013.08.068>, <http://www.sciencedirect.com/science/article/pii/S1352231013006894>, 2013.



- 565 Dunlea, E. J., Herndon, S. C., Nelson, D. D., Volkamer, R. M., San Martini, F., Sheehy, P. M., Zahniser, M. S., Shorter, J. H., Wormhoudt, J. C., Lamb, B. K., Allwine, E. J., Gaffney, J. S., Marley, N. A., Grutter, M., Marquez, C., Blanco, S., Cardenas, B., Retama, A., Ramos Villegas, C. R., Kolb, C. E., Molina, L. T., and Molina, M. J.: Evaluation of nitrogen dioxide chemiluminescence mon-
itors in a polluted urban environment, *Atmos. Chem. Phys.*, 7, 2691–2704, <https://doi.org/https://doi.org/10.5194/acp-7-2691-2007>, <https://www.atmos-chem-phys.net/7/2691/2007/>, 2007.
- 570 Fehsenfeld, F. C., Drummond, J. W., Roychowdhury, U. K., Galvin, P. J., Williams, E. J., Buhr, M. P., Parrish, D. D., Hübler, G., Langford, A. O., Calvert, J. G., Ridley, B. A., Grahek, F., Heikes, B. G., Kok, G. L., Shetter, J. D., Walega, J. G., Elsworth, C. M., Norton, R. B., Fahey, D. W., Murphy, P. C., Hovermale, C., Mohnen, V. A., Demerjian, K. L., Mackay, G. I., and Schiff, H. I.: Inter-
comparison of NO₂ measurement techniques, *J. Geophys. Res. Atmos.*, 95, 3579–3597, <https://doi.org/10.1029/JD095iD04p03579>, <https://agupubs.onlinelibrary.wiley.com/doi/abs/10.1029/JD095iD04p03579>, 1990.
- Geddes, J. A. and Martin, R. V.: Global deposition of total reactive nitrogen oxides from 1996 to 2014 constrained with satellite ob-
servations of NO₂ columns, *Atmos. Chem. Phys.*, 17, 10071–10091, <https://doi.org/https://doi.org/10.5194/acp-17-10071-2017>, <https://www.atmos-chem-phys.net/17/10071/2017/>, 2017.
- 575 Gelaro, R., McCarty, W., Suárez, M. J., Todling, R., Molod, A., Takacs, L., Randles, C. A., Darmenov, A., Bosilovich, M. G., Reichle, R., Wargan, K., Coy, L., Cullather, R., Draper, C., Akella, S., Buchard, V., Conaty, A., da Silva, A. M., Gu, W., Kim, G.-K., Koster, R., Lucchesi, R., Merkova, D., Nielsen, J. E., Partyka, G., Pawson, S., Putman, W., Rienecker, M., Schubert, S. D., Sienkiewicz, M., and Zhao, B.: The Modern-Era Retrospective Analysis for Research and Applications, Version 2 (MERRA-2), *J. Clim.*, 30, 5419–5454, <https://doi.org/10.1175/JCLI-D-16-0758.1>, <https://journals.ametsoc.org/doi/full/10.1175/JCLI-D-16-0758.1>, 2017.
- 580 Ghude, S. D., Lal, D. M., Beig, G., van der A, R., and Sable, D.: Rain-Induced Soil NO_x Emission From India During the Onset of the Summer Monsoon: A Satellite Perspective, *Journal of Geophysical Research: Atmospheres*, 115, <https://doi.org/10.1029/2009JD013367>, <https://agupubs.onlinelibrary.wiley.com/doi/abs/10.1029/2009JD013367>, 2010.
- Ghude, S. D., Kulkarni, S. H., Jena, C., Pfister, G. G., Beig, G., Fadnavis, S., and A, R. J. v. d.: Application of satellite observations for
identifying regions of dominant sources of nitrogen oxides over the Indian Subcontinent, *J. Geophys. Res. Atmos.*, 118, 1075–1089,
585 <https://doi.org/10.1029/2012JD017811>, <https://agupubs.onlinelibrary.wiley.com/doi/abs/10.1029/2012JD017811>, 2013a.
- Ghude, S. D., Pfister, G. G., Jena, C., A, R. J. v. d., Emmons, L. K., and Kumar, R.: Satellite constraints of nitrogen oxide (NO_x) emissions
from India based on OMI observations and WRF-Chem simulations, *Geophys. Res. Lett.*, 40, 423–428, <https://doi.org/10.1002/grl.50065>, <https://agupubs.onlinelibrary.wiley.com/doi/abs/10.1002/grl.50065>, 2013b.
- 590 Goldberg, D. L., Lamsal, L. N., Loughner, C. P., Swartz, W. H., Lu, Z., and Streets, D. G.: A high-resolution and observationally
constrained OMI NO₂ satellite retrieval, *Atmos. Chem. Phys.*, 17, 11403–11421, <https://doi.org/10.5194/acp-17-11403-2017>, <https://www.atmos-chem-phys.net/17/11403/2017/>, 2017.
- Goldberg, D. L., Saide, P. E., Lamsal, L. N., Foy, B. d., Lu, Z., Woo, J.-H., Kim, Y., Kim, J., Gao, M., Carmichael, G., and Streets, D. G.: A
top-down assessment using OMI NO₂ suggests an underestimate in the NO_x emissions inventory in Seoul, South Korea, during KORUS-
AQ, *Atmos. Chem. Phys.*, 19, 1801–1818, <https://doi.org/https://doi.org/10.5194/acp-19-1801-2019>, <https://www.atmos-chem-phys.net/19/1801/2019/acp-19-1801-2019.html>, 2019.
- 595 Grell, G. A., Peckham, S. E., Schmitz, R., McKeen, S. A., Frost, G., Skamarock, W. C., and Eder, B.: Fully coupled “online” chemistry
within the WRF model, *Atmos. Environ.*, 39, 6957–6975, <https://doi.org/10.1016/j.atmosenv.2005.04.027>, <http://www.sciencedirect.com/science/article/pii/S1352231005003560>, 2005.



- Hains, J. C., Boersma, K. F., Kroon, M., Dirksen, R. J., Cohen, R. C., Perring, A. E., Bucsela, E., Volten, H., Swart, D. P. J., Richter, A.,
600 Wittrock, F., Schoenhardt, A., Wagner, T., Ibrahim, O. W., Roozendael, M. v., Pinaridi, G., Gleason, J. F., Veefkind, J. P., and Levelt, P.:
Testing and improving OMI DOMINO tropospheric NO₂ using observations from the DANDELIONS and INTEX-B validation cam-
paigns, *J. Geophys. Res. Atmos.*, 115, D05 301, <https://doi.org/10.1029/2009JD012399>, <https://agupubs.onlinelibrary.wiley.com/doi/abs/10.1029/2009JD012399>, 2010.
- Herman, J., Cede, A., Spinei, E., Mount, G., Tzortziou, M., and Abuhassan, N.: NO₂ column amounts from ground-based Pandora and
605 MFDOAS spectrometers using the direct-sun DOAS technique: Intercomparisons and application to OMI validation, *J. Geophys. Res. Atmos.*, 114, D13 307, <https://doi.org/10.1029/2009JD011848>, <https://agupubs.onlinelibrary.wiley.com/doi/abs/10.1029/2009JD011848>, 2009.
- Herman, J., Spinei, E., Fried, A., Kim, J., Kim, J., Kim, W., Cede, A., Abuhassan, N., and Segal-Rozenhaimer, M.: NO₂ and HCHO
610 measurements in Korea from 2012 to 2016 from Pandora spectrometer instruments compared with OMI retrievals and with aircraft
measurements during the KORUS-AQ campaign, *Atmos. Meas. Tech.*, 11, 4583–4603, <https://doi.org/10.5194/amt-11-4583-2018>, <https://www.atmos-meas-tech.net/11/4583/2018/>, 2018.
- Herron-Thorpe, F. L., Lamb, B. K., Mount, G. H., and Vaughan, J. K.: Evaluation of a regional air quality forecast model
for tropospheric NO₂ columns using the OMI/Aura satellite tropospheric NO₂ product, *Atmos. Chem. Phys.*, 10, 8839–8854,
<https://doi.org/https://doi.org/10.5194/acp-10-8839-2010>, <https://www.atmos-chem-phys.net/10/8839/2010/>, 2010.
- 615 Hilboll, A., Richter, A., and Burrows, J. P.: Long-term changes of tropospheric NO₂ over megacities derived from multiple satellite instru-
ments, *Atmos. Chem. Phys.*, 13, 4145–4169, <https://doi.org/https://doi.org/10.5194/acp-13-4145-2013>, <https://www.atmos-chem-phys.net/13/4145/2013/>, 2013.
- Hong, S.-Y., Noh, Y., and Dudhia, J.: A new vertical diffusion package with an explicit treatment of entrainment processes, *Mon. Wea. Rev.*,
134, 2318–2341, <https://doi.org/10.1175/MWR3199.1>, <https://journals.ametsoc.org/doi/full/10.1175/MWR3199.1>, 2006.
- 620 Huijnen, V., Eskes, H. J., Poupkou, A., Elbern, H., Boersma, K. F., Foret, G., Sofiev, M., Valdebenito, A., Flemming, J., Stein, O., Gross,
A., Robertson, L., D'Isidoro, M., Kioutsioukis, I., Friese, E., Amstrup, B., Bergstrom, R., Strunk, A., Vira, J., Zyryanov, D., Maurizi,
A., Melas, D., Peuch, V.-H., and Zerefos, C.: Comparison of OMI NO₂ tropospheric columns with an ensemble of global and European
regional air quality models, *Atmos. Chem. Phys.*, 10, 3273–3296, <https://doi.org/https://doi.org/10.5194/acp-10-3273-2010>, <https://www.atmos-chem-phys.net/10/3273/2010/>, 2010.
- 625 Ialongo, I., Herman, J., Krotkov, N., Lamsal, L., Boersma, K. F., Hovila, J., and Tamminen, J.: Comparison of OMI NO₂ obser-
vations and their seasonal and weekly cycles with ground-based measurements in Helsinki, *Atmos. Meas. Tech.*, 9, 5203–5212,
<https://doi.org/https://doi.org/10.5194/amt-9-5203-2016>, <https://www.atmos-meas-tech.net/9/5203/2016/>, 2016.
- Irie, H., Boersma, K. F., Kanaya, Y., Takashima, H., Pan, X., and Wang, Z. F.: Quantitative bias estimates for tropospheric NO₂ columns
retrieved from SCIAMACHY, OMI, and GOME-2 using a common standard for East Asia, *Atmos. Meas. Tech.*, 5, 2403–2411,
630 <https://doi.org/10.5194/amt-5-2403-2012>, <https://www.atmos-meas-tech.net/5/2403/2012/>, 2012.
- Jaeglé, L., Steinberger, L., Martin, R. V., and Chance, K.: Global partitioning of NO_x sources using satellite observations: Relative roles
of fossil fuel combustion, biomass burning and soil emissions, *Faraday Discuss.*, 130, 407–423, <https://doi.org/10.1039/B502128F>, <https://pubs.rsc.org/en/content/articlelanding/2005/fd/b502128f>, 2005.
- Kebabian, P. L., Wood, E. C., Herndon, S. C., and Freedman, A.: A practical alternative to chemiluminescence-based detection of nitrogen
635 dioxide: cavity attenuated phase shift spectroscopy, *Environ. Sci. Technol.*, 42, 6040–6045, <https://doi.org/10.1021/es703204j>, <https://doi.org/10.1021/es703204j>, 2008.



- Kim, H. C., Lee, P., Judd, L., Pan, L., and Lefer, B.: OMI NO₂ column densities over North American urban cities: the effect of satellite footprint resolution, *Geosci. Model Dev.*, 9, 1111–1123, <https://doi.org/10.5194/gmd-9-1111-2016>, <https://www.geosci-model-dev.net/9/1111/2016/>, 2016.
- 640 Kim, H. C., Lee, S.-M., Chai, T., Ngan, F., Pan, L., and Lee, P.: A conservative downscaling of satellite-detected chemical compositions: NO₂ column densities of OMI, GOME-2, and CMAQ, *Remote Sensing*, 10, 1001, <https://doi.org/10.3390/rs10071001>, <https://www.mdpi.com/2072-4292/10/7/1001>, 2018.
- Kim, S.-W., Heckel, A., Frost, G. J., Richter, A., Gleason, J., Burrows, J. P., McKeen, S., Hsie, E.-Y., Granier, C., and Trainer, M.: NO₂ columns in the western United States observed from space and simulated by a regional chemistry model and their implications for NO_x emissions, *J. Geophys. Res. Atmos.*, 114, D11 301, <https://doi.org/10.1029/2008JD011343>, <https://agupubs.onlinelibrary.wiley.com/doi/abs/10.1029/2008JD011343>, 2009.
- 645 Kononov, I. B., Beekmann, M., Richter, A., and Burrows, J. P.: Inverse modelling of the spatial distribution of NO_x emissions on a continental scale using satellite data, *Atmos. Chem. Phys.*, 6, 1747–1770, <https://doi.org/https://doi.org/10.5194/acp-6-1747-2006>, <https://www.atmos-chem-phys.net/6/1747/2006/>, 2006.
- 650 Krotkov, N. A., McLinden, C. A., Li, C., Lamsal, L. N., Celarier, E. A., Marchenko, S. V., Swartz, W. H., Bucsela, E. J., Joiner, J., Duncan, B. N., Boersma, K. F., Veefkind, J. P., Levelt, P. F., Fioletov, V. E., Dickerson, R. R., He, H., Lu, Z., and Streets, D. G.: Aura OMI observations of regional SO₂ and NO₂ pollution changes from 2005 to 2015, *Atmos. Chem. Phys.*, 16, 4605–4629, <https://doi.org/https://doi.org/10.5194/acp-16-4605-2016>, <https://www.atmos-chem-phys.net/16/4605/2016/>, 2016.
- Krotkov, N. A., Lamsal, L. N., Celarier, E. A., Swartz, W. H., Marchenko, S. V., Bucsela, E. J., Chan, K. L., Wenig, M., and Zara, M.: The version 3 OMI NO₂ standard product, *Atmos. Meas. Tech.*, 10, 3133–3149, <https://doi.org/https://doi.org/10.5194/amt-10-3133-2017>, <https://www.atmos-meas-tech.net/10/3133/2017/amt-10-3133-2017.html>, 2017.
- 655 Lamsal, L. N., Martin, R. V., Donkelaar, A. v., Steinbacher, M., Celarier, E. A., Bucsela, E., Dunlea, E. J., and Pinto, J. P.: Ground-level nitrogen dioxide concentrations inferred from the satellite-borne Ozone Monitoring Instrument, *J. Geophys. Res. Atmos.*, 113, D16 308, <https://doi.org/10.1029/2007JD009235>, <https://agupubs.onlinelibrary.wiley.com/doi/abs/10.1029/2007JD009235>, 2008.
- 660 Lamsal, L. N., Martin, R. V., Donkelaar, A. v., Celarier, E. A., Bucsela, E. J., Boersma, K. F., Dirksen, R., Luo, C., and Wang, Y.: Indirect validation of tropospheric nitrogen dioxide retrieved from the OMI satellite instrument: Insight into the seasonal variation of nitrogen oxides at northern midlatitudes, *J. Geophys. Res. Atmos.*, 115, D05 302, <https://doi.org/10.1029/2009JD013351>, <https://agupubs.onlinelibrary.wiley.com/doi/abs/10.1029/2009JD013351>, 2010.
- Lamsal, L. N., Martin, R. V., Padmanabhan, A., van Donkelaar, A., Zhang, Q., Sioris, C. E., Chance, K., Kurosu, T. P., and Newchurch, M. J.: Application of satellite observations for timely updates to global anthropogenic NO_x emission inventories, *Geophysical Research Letters*, 38, <https://doi.org/10.1029/2010GL046476>, <https://agupubs.onlinelibrary.wiley.com/doi/abs/10.1029/2010GL046476>, 2011.
- 665 Lamsal, L. N., Krotkov, N. A., Celarier, E. A., Swartz, W. H., Pickering, K. E., Bucsela, E. J., Gleason, J. F., Martin, R. V., Philip, S., Irie, H., Cede, A., Herman, J., Weinheimer, A., Szykman, J. J., and Knepp, T. N.: Evaluation of OMI operational standard NO₂ column retrievals using in situ and surface-based NO₂ observations, *Atmos. Chem. Phys.*, 14, 11 587–11 609, <https://doi.org/10.5194/acp-14-11587-2014>, <https://www.atmos-chem-phys.net/14/11587/2014/>, 2014.
- 670 Lamsal, L. N., Duncan, B. N., Yoshida, Y., Krotkov, N. A., Pickering, K. E., Streets, D. G., and Lu, Z.: U.S. NO₂ trends (2005–2013): EPA Air Quality System (AQS) data versus improved observations from the Ozone Monitoring Instrument (OMI), *Atmos. Environ.*, 110, 130–143, <https://doi.org/10.1016/j.atmosenv.2015.03.055>, <http://www.sciencedirect.com/science/article/pii/S1352231015002794>, 2015.



- Lamsal, L. N., Janz, S. J., Krotkov, N. A., Pickering, K. E., Spurr, R. J. D., Kowalewski, M. G., Loughner, C. P., Crawford, J. H., Swartz, W. H., and Herman, J. R.: High-resolution NO₂ observations from the Airborne Compact Atmospheric Mapper: retrieval and validation, *J. Geophys. Res. Atmos.*, 122, 1953–1970, <https://doi.org/10.1002/2016JD025483>, <https://agupubs.onlinelibrary.wiley.com/doi/abs/10.1002/2016JD025483>, 2017.
- Laughner, J. L., Zare, A., and Cohen, R. C.: Effects of daily meteorology on the interpretation of space-based remote sensing of NO₂, *Atmos. Chem. Phys.*, 16, 15 247–15 264, <https://doi.org/https://doi.org/10.5194/acp-16-15247-2016>, <https://www.atmos-chem-phys.net/16/15247/2016/acp-16-15247-2016.html>, 2016.
- Laughner, J. L., Zhu, Q., and Cohen, R. C.: Evaluation of version 3.0B of the BEHR OMI NO₂ product, *Atmos. Meas. Tech.*, 12, 129–146, <https://doi.org/10.5194/amt-12-129-2019>, <https://www.atmos-meas-tech.net/12/129/2019/>, 2019.
- Levelt, P. F., Oord, G. H. J. v. d., Dobber, M. R., Malkki, A., Huib Visser, Johan de Vries, Stammes, P., Lundell, J. O. V., and Saari, H.: The ozone monitoring instrument, *IEEE Trans. Geosci. Remote Sens.*, 44, 1093–1101, <https://doi.org/10.1109/TGRS.2006.872333>, 2006.
- Levelt, P. F., Joiner, J., Tamminen, J., Veefkind, J. P., Bhartia, P. K., Stein Zweers, D. C., Duncan, B. N., Streets, D. G., Eskes, H., A, R. v. d., McLinden, C., Fioletov, V., Carn, S., Laatz, J. d., DeLand, M., Marchenko, S., McPeters, R., Ziemke, J., Fu, D., Liu, X., Pickering, K., Apituley, A., González Abad, G., Arola, A., Boersma, F., Chan Miller, C., Chance, K., Graaf, M. d., Hakkarainen, J., Hassinen, S., Ialongo, I., Kleipool, Q., Krotkov, N., Li, C., Lamsal, L., Newman, P., Nowlan, C., Suleiman, R., Tilstra, L. G., Torres, O., Wang, H., and Wargan, K.: The Ozone Monitoring Instrument: overview of 14 years in space, *Atmos. Chem. Phys.*, 18, 5699–5745, <https://doi.org/https://doi.org/10.5194/acp-18-5699-2018>, <https://www.atmos-chem-phys.net/18/5699/2018/>, 2018.
- Lin, J.-T.: Satellite constraint for emissions of nitrogen oxides from anthropogenic, lightning and soil sources over East China on a high-resolution grid, *Atmos. Chem. Phys.*, 12, 2881–2898, <https://doi.org/https://doi.org/10.5194/acp-12-2881-2012>, <https://www.atmos-chem-phys.net/12/2881/2012/>, 2012.
- Lin, J.-T., McElroy, M. B., and Boersma, K. F.: Constraint of anthropogenic NO_x emissions in China from different sectors: a new methodology using multiple satellite retrievals, *Atmos. Chem. Phys.*, 10, 63–78, <https://doi.org/https://doi.org/10.5194/acp-10-63-2010>, <https://www.atmos-chem-phys.net/10/63/2010/>, 2010.
- Lin, J.-T., Martin, R. V., Boersma, K. F., Sneep, M., Stammes, P., Spurr, R., Wang, P., Van Roozendaal, M., Clémer, K., and Irie, H.: Retrieving tropospheric nitrogen dioxide from the Ozone Monitoring Instrument: effects of aerosols, surface reflectance anisotropy, and vertical profile of nitrogen dioxide, *Atmos. Chem. Phys.*, 14, 1441–1461, <https://doi.org/https://doi.org/10.5194/acp-14-1441-2014>, <https://www.atmos-chem-phys.net/14/1441/2014/acp-14-1441-2014.html>, 2014.
- Lin, J.-T., Liu, M.-Y., Xin, J.-Y., Boersma, K. F., Spurr, R., Martin, R., and Zhang, Q.: Influence of aerosols and surface reflectance on satellite NO₂ retrieval: seasonal and spatial characteristics and implications for NO_x emission constraints, *Atmos. Chem. Phys.*, 15, 11 217–11 241, <https://doi.org/https://doi.org/10.5194/acp-15-11217-2015>, <https://www.atmos-chem-phys.net/15/11217/2015/acp-15-11217-2015.html>, 2015.
- Liu, F., van der A, R. J., Eskes, H., Ding, J., and Mijling, B.: Evaluation of modeling NO₂ concentrations driven by satellite-derived and bottom-up emission inventories using in situ measurements over China, *Atmos. Chem. Phys.*, 18, 4171–4186, <https://doi.org/10.5194/acp-18-4171-2018>, <https://www.atmos-chem-phys.net/18/4171/2018/>, 2018.
- Liu, M., Lin, J., Boersma, K. F., Pinardi, G., Wang, Y., Chimot, J., Wagner, T., Xie, P., Eskes, H., Van Roozendaal, M., Hendrick, F., Wang, P., Wang, T., Yan, Y., Chen, L., and Ni, R.: Improved aerosol correction for OMI tropospheric NO₂ retrieval over East Asia: constraint from CALIOP aerosol vertical profile, *Atmos. Meas. Tech.*, 12, 1–21, <https://doi.org/10.5194/amt-12-1-2019>, <https://www.atmos-meas-tech.net/12/1/2019/>, 2019.



- Lorente, A., Boersma, K. F., Stammes, P., Tilstra, L. G., Richter, A., Yu, H., Kharbouche, S., and Muller, J.-P.: The importance of surface reflectance anisotropy for cloud and NO₂ retrievals from GOME-2 and OMI, *Atmos. Meas. Tech.*, 11, 4509–4529, <https://doi.org/https://doi.org/10.5194/amt-11-4509-2018>, <https://www.atmos-meas-tech.net/11/4509/2018/>, 2018.
- 715 Loughner, C. P., Tzortziou, M., Follette-Cook, M., Pickering, K. E., Goldberg, D., Satam, C., Weinheimer, A., Crawford, J. H., Knapp, D. J., Montzka, D. D., Diskin, G. S., and Dickerson, R. R.: Impact of bay-breeze circulations on surface air quality and boundary layer export, *J. Appl. Meteor. Clim.*, 53, 1697–1713, <https://doi.org/10.1175/JAMC-D-13-0323.1>, <http://journals.ametsoc.org/doi/abs/10.1175/JAMC-D-13-0323.1>, 2014.
- Lu, Z. and Streets, D. G.: Increase in NO_x emissions from Indian thermal power plants during 1996–2010: unit-based inventories and multi-satellite observations, *Environ. Sci. Technol.*, 46, 7463–7470, <https://doi.org/10.1021/es300831w>, <https://doi.org/10.1021/es300831w>, 2012.
- 720 Marchenko, S., Krotkov, N. A., Lamsal, L. N., Celarier, E. A., Swartz, W. H., and Bucsele, E. J.: Revising the slant column density retrieval of nitrogen dioxide observed by the Ozone Monitoring Instrument, *J. Geophys. Res. Atmos.*, 120, 5670–5692, <https://doi.org/10.1002/2014JD022913>, <https://agupubs.onlinelibrary.wiley.com/doi/abs/10.1002/2014JD022913>, 2015.
- 725 Martin, R. V., Chance, K., Jacob, D. J., Kurosu, T. P., Spurr, R. J. D., Bucsele, E., Gleason, J. F., Palmer, P. I., Bey, I., Fiore, A. M., Li, Q., Yantosca, R. M., and Koelemeijer, R. B. A.: An improved retrieval of tropospheric nitrogen dioxide from GOME, *J. Geophys. Res. Atmos.*, 107, ACH 9–1–ACH 9–21, <https://doi.org/10.1029/2001JD001027>, <https://agupubs.onlinelibrary.wiley.com/doi/abs/10.1029/2001JD001027>, 2002.
- Martin, R. V., Jacob, D. J., Chance, K., Kurosu, T. P., Palmer, P. I., and Evans, M. J.: Global inventory of nitrogen oxide emissions constrained by space-based observations of NO₂ columns, *J. Geophys. Res. Atmos.*, 108, 4537, <https://doi.org/10.1029/2003JD003453>, <https://agupubs.onlinelibrary.wiley.com/doi/abs/10.1029/2003JD003453>, 2003.
- 730 McLinden, C. A., Fioletov, V., Boersma, K. F., Kharol, S. K., Krotkov, N., Lamsal, L., Makar, P. A., Martin, R. V., Veefkind, J. P., and Yang, K.: Improved satellite retrievals of NO₂ and SO₂ over the Canadian oil sands and comparisons with surface measurements, *Atmos. Chem. Phys.*, 14, 3637–3656, <https://doi.org/10.5194/acp-14-3637-2014>, <https://www.atmos-chem-phys.net/14/3637/2014/>, 2014.
- 735 Mebust, A. K. and Cohen, R. C.: Observations of a seasonal cycle in NO_x emissions from fires in African woody savannas, *Geophys. Res. Lett.*, 40, 1451–1455, <https://doi.org/10.1002/grl.50343>, <https://agupubs.onlinelibrary.wiley.com/doi/abs/10.1002/grl.50343>, 2013.
- Miyazaki, K., Eskes, H., Sudo, K., Boersma, K. F., Bowman, K., and Kanaya, Y.: Decadal changes in global surface NO_x emissions from multi-constituent satellite data assimilation, *Atmos. Chem. Phys.*, 17, 807–837, <https://doi.org/https://doi.org/10.5194/acp-17-807-2017>, <https://www.atmos-chem-phys.net/17/807/2017/>, 2017.
- 740 Murray, L. T., Jacob, D. J., Logan, J. A., Hudman, R. C., and Koshak, W. J.: Optimized regional and interannual variability of lightning in a global chemical transport model constrained by LIS/OTD satellite data, *J. Geophys. Res. Atmos.*, 117, D20307, <https://doi.org/10.1029/2012JD017934>, <https://agupubs.onlinelibrary.wiley.com/doi/abs/10.1029/2012JD017934>, 2012.
- Murray, L. T., Mickley, L. J., Kaplan, J. O., Sofen, E. D., Pfeiffer, M., and Alexander, B.: Factors controlling variability in the oxidative capacity of the troposphere since the Last Glacial Maximum, *Atmos. Chem. Phys.*, 14, 3589–3622, <https://doi.org/https://doi.org/10.5194/acp-14-3589-2014>, <https://www.atmos-chem-phys.net/14/3589/2014/>, 2014.
- 745 Noguchi, K., Richter, A., Rozanov, V., Rozanov, A., Burrows, J. P., Irie, H., and Kita, K.: Effect of surface BRDF of various land cover types on geostationary observations of tropospheric NO₂, *Atmos. Meas. Tech.*, 7, 3497–3508, <https://doi.org/10.5194/amt-7-3497-2014>, <https://www.atmos-meas-tech.net/7/3497/2014/>, 2014.



- Novotny, E. V., Bechle, M. J., Millet, D. B., and Marshall, J. D.: National satellite-based land-use regression: NO₂ in the United States, Environ. Sci. Technol., 45, 4407–4414, <https://doi.org/10.1021/es103578x>, <https://doi.org/10.1021/es103578x>, 2011.
- 750 Nowlan, C. R., Martin, R. V., Philip, S., Lamsal, L. N., Krotkov, N. A., Marais, E. A., Wang, S., and Zhang, Q.: Global dry deposition of nitrogen dioxide and sulfur dioxide inferred from space-based measurements, Global Biogeochemical Cycles, 28, 1025–1043, <https://doi.org/10.1002/2014GB004805>, <https://agupubs.onlinelibrary.wiley.com/doi/abs/10.1002/2014GB004805>, 2014.
- Nowlan, C. R., Liu, X., Leitch, J. W., Chance, K., González Abad, G., Liu, C., Zoogman, P., Cole, J., Delker, T., Good, W., Murcay, F., Ruppert, L., Soo, D., Follette-Cook, M. B., Janz, S. J., Kowalewski, M. G., Loughner, C. P., Pickering, K. E., Herman, J. R., Beaver, M. R., Long, R. W., Szykman, J. J., Judd, L. M., Kelley, P., Luke, W. T., Ren, X., and Al-Saadi, J. A.: Nitrogen dioxide observations from the Geostationary Trace gas and Aerosol Sensor Optimization (GeoTASO) airborne instrument: Retrieval algorithm and measurements during DISCOVER-AQ Texas 2013, Atmos. Meas. Tech., 9, 2647–2668, <https://doi.org/https://doi.org/10.5194/amt-9-2647-2016>, <https://www.atmos-meas-tech.net/9/2647/2016/>, 2016.
- 755 760 Nowlan, C. R., Liu, X., Janz, S. J., Kowalewski, M. G., Chance, K., Follette-Cook, M. B., Fried, A., González Abad, G., Herman, J. R., Judd, L. M., Kwon, H.-A., Loughner, C. P., Pickering, K. E., Richter, D., Spinei, E., Walega, J., Weibring, P., and Weinheimer, A. J.: Nitrogen dioxide and formaldehyde measurements from the GEOstationary Coastal and Air Pollution Events (GEO-CAPE) Airborne Simulator over Houston, Texas, Atmos. Meas. Tech., 11, 5941–5964, <https://doi.org/10.5194/amt-11-5941-2018>, <https://www.atmos-meas-tech.net/11/5941/2018/>, 2018.
- 765 Pfister, G. G., Walters, S., Lamarque, J.-F., Fast, J., Barth, M. C., Wong, J., Done, J., Holland, G., and Bruyère, C. L.: Projections of future summertime ozone over the U.S., J. Geophys. Res. Atmos., 119, 5559–5582, <https://doi.org/10.1002/2013JD020932>, <https://agupubs.onlinelibrary.wiley.com/doi/abs/10.1002/2013JD020932>, 2014.
- Pickering, K. E., Bucselá, E., Allen, D., Ring, A., Holzworth, R., and Krotkov, N.: Estimates of lightning NO_x production based on OMI NO₂ observations over the Gulf of Mexico, J. Geophys. Res. Atmos., 121, 8668–8691, <https://doi.org/10.1002/2015JD024179>, <https://agupubs.onlinelibrary.wiley.com/doi/abs/10.1002/2015JD024179>, 2016.
- 770 Pleim, J. E.: A Combined Local and Nonlocal Closure Model for the Atmospheric Boundary Layer. Part II: Application and Evaluation in a Mesoscale Meteorological Model, Journal of Applied Meteorology and Climatology, 46, 1396–1409, <https://doi.org/10.1175/JAM2534.1>, <https://doi.org/10.1175/JAM2534.1>, 2007.
- Pleim, J. E. and Xiu, A.: Development of a Land Surface Model. Part II: Data Assimilation, Journal of Applied Meteorology, 42, 1811–1822, [https://doi.org/10.1175/1520-0450\(2003\)042<1811:DOALSM>2.0.CO;2](https://doi.org/10.1175/1520-0450(2003)042<1811:DOALSM>2.0.CO;2), [https://doi.org/10.1175/1520-0450\(2003\)042<1811:DOALSM>2.0.CO;2](https://doi.org/10.1175/1520-0450(2003)042<1811:DOALSM>2.0.CO;2), 2003.
- 775 Richter, A., Burrows, J. P., Nüß, H., Granier, C., and Niemeier, U.: Increase in tropospheric nitrogen dioxide over China observed from space, Nature, 437, 129–132, <https://doi.org/10.1038/nature04092>, <https://www.nature.com/articles/nature04092>, 2005.
- Ridley, B. A. and Grahek, F. E.: A small, low flow, high sensitivity reaction vessel for NO chemiluminescence detectors, J. Atmos. Oceanic Technol., 7, 307–311, [https://doi.org/10.1175/1520-0426\(1990\)007<0307:ASLFHS>2.0.CO;2](https://doi.org/10.1175/1520-0426(1990)007<0307:ASLFHS>2.0.CO;2), <https://journals.ametsoc.org/doi/abs/10.1175/1520-0426%281990%29007%3C0307%3AASLFHS%3E2.0.CO%3B2>, 1990.
- 780 Russell, A. R., Valin, L. C., Bucselá, E. J., Wenig, M. O., and Cohen, R. C.: Space-based constraints on spatial and temporal patterns of NO_x emissions in California, 2005–2008, Environ. Sci. Technol., 44, 3608–3615, <https://doi.org/10.1021/es903451j>, <https://doi.org/10.1021/es903451j>, 2010.



- 785 Russell, A. R., Valin, L. C., and Cohen, R. C.: Trends in OMI NO₂ observations over the United States: effects of emission control technology and the economic recession, *Atmos. Chem. Phys.*, 12, 12 197–12 209, <https://doi.org/10.5194/acp-12-12197-2012>, <https://www.atmos-chem-phys.net/12/12197/2012/>, 2012.
- Saide, P. E., Kim, J., Song, C. H., Choi, M., Cheng, Y., and Carmichael, G. R.: Assimilation of next generation geostationary aerosol optical depth retrievals to improve air quality simulations, *Geophys. Res. Lett.*, 41, 9188–9196, <https://doi.org/10.1002/2014GL062089>,
790 <https://agupubs.onlinelibrary.wiley.com/doi/abs/10.1002/2014GL062089>, 2014.
- Saide, P. E., Gao, M., Lu, Z., Goldberg, D., Streets, D. G., Woo, J.-H., Beyersdorf, A., Thornhill, K. L., Hair, J. W., Nehrir, A. R., Jimenez, J.-L., Nault, B. A., Campuzano-Jost, P., Dibb, J., Heim, E., Lamb, K. D., Schwarz, J. P., Perring, A. E., Kim, J., Choi, M., Holben, B., Pfister, G., Hodzic, A., Carmichael, G. R., Emmons, L., and Crawford, J. H.: Understanding and improving model representation of aerosol optical properties for a Chinese haze event measured by KORUS-AQ, in preparation.
- 795 Schaub, D., Brunner, D., Boersma, K. F., Keller, J., Folini, D., Buchmann, B., Berresheim, H., and Staehelin, J.: SCIAMACHY tropospheric NO₂ over Switzerland: estimates of NO_x lifetimes and impact of the complex Alpine topography on the retrieval, *Atmos. Chem. Phys.*, 7, 5971–5987, <https://doi.org/10.5194/acp-7-5971-2007>, <https://www.atmos-chem-phys.net/7/5971/2007/>, 2007.
- Schenkeveld, V. M. E., Jaross, G., Marchenko, S., Haffner, D., Kleipool, Q. L., Rozemeijer, N. C., Veefkind, J. P., and Levelt, P. F.: In-flight performance of the Ozone Monitoring Instrument, *Atmos. Meas. Tech.*, 10, 1957–1986, <https://doi.org/10.5194/amt-10-1957-2017>,
800 <https://www.atmos-meas-tech.net/10/1957/2017/amt-10-1957-2017.html>, 2017.
- Schreier, S. F., Richter, A., Schepaschenko, D., Shvidenko, A., Hilboll, A., and Burrows, J. P.: Differences in satellite-derived NO_x emission factors between Eurasian and North American boreal forest fires, *Atmos. Environ.*, 121, 55–65, <https://doi.org/10.1016/j.atmosenv.2014.08.071>, <http://www.sciencedirect.com/science/article/pii/S1352231014006827>, 2015.
- Skamarock, W. C., Klemp, J. B., Dudhia, J., Gill, D. O., Barker, D. M., Wang, W., and Powers, J. G.: A description of the Advanced Research WRF version 3. NCAR Technical note -475+STR, NCAR, Boulder, Colorado, USA, 2008.
805
- Sluis, W. W., Allaart, M. A. F., PETERS, A. J. M., and Gast, L. F. L.: The development of a nitrogen dioxide sonde, *Atmos. Meas. Tech.*, 3, 1753–1762, <https://doi.org/10.5194/amt-3-1753-2010>, <https://www.atmos-meas-tech.net/3/1753/2010/>, 2010.
- Spinei, E., Cede, A., Swartz, W. H., Herman, J., and Mount, G. H.: The use of NO₂ absorption cross section temperature sensitivity to derive NO₂ profile temperature and stratospheric–tropospheric column partitioning from visible direct-sun DOAS measurements, *Atmos. Meas. Tech.*, 7, 4299–4316, <https://doi.org/10.5194/amt-7-4299-2014>, <https://www.atmos-meas-tech.net/7/4299/2014/>, 2014.
810
- Steinbacher, M., Zellweger, C., Schwarzenbach, B., Bugmann, S., Buchmann, B., Ordóñez, C., Prevot, A. S. H., and Hueglin, C.: Nitrogen oxide measurements at rural sites in Switzerland: Bias of conventional measurement techniques, *J. Geophys. Res. Atmos.*, 112, D11 307, <https://doi.org/10.1029/2006JD007971>, <https://agupubs.onlinelibrary.wiley.com/doi/abs/10.1029/2006JD007971>, 2007.
- Strahan, S. E., Douglass, A. R., and Newman, P. A.: The contributions of chemistry and transport to low arctic ozone in March 2011 derived from Aura MLS observations, *J. Geophys. Res. Atmos.*, 118, 1563–1576, <https://doi.org/10.1002/jgrd.50181>, <https://agupubs.onlinelibrary.wiley.com/doi/abs/10.1002/jgrd.50181>, 2013.
815
- Strahan, S. E., Douglass, A. R., and Steenrod, S. D.: Chemical and dynamical impacts of stratospheric sudden warmings on Arctic ozone variability, *J. Geophys. Res. Atmos.*, 121, 11 836–11 851, <https://doi.org/10.1002/2016JD025128>, <https://agupubs.onlinelibrary.wiley.com/doi/abs/10.1002/2016JD025128>, 2016.
- 820 Strode, S. A., Rodriguez, J. M., Logan, J. A., Cooper, O. R., Witte, J. C., Lamsal, L. N., Damon, M., Aartsen, B. V., Steenrod, S. D., and Strahan, S. E.: Trends and variability in surface ozone over the United States, *J. Geophys. Res. Atmos.*, 120, 9020–9042, <https://doi.org/10.1002/2014JD022784>, <https://agupubs.onlinelibrary.wiley.com/doi/abs/10.1002/2014JD022784>, 2015.



- 825 Tewari, M., Chen, F., Wang, W., Dudhia, J., LeMone, M., Mitchell, K., Ek, M., Gayno, G., Wegiel, J., and Cuenca, R.: Implementation and verification of the unified NOAA land surface model in the WRF model, vol. 1115, American Meteorological Society, Seattle, Washington, USA, 2004.
- Thornton, J. A., Wooldridge, P. J., and Cohen, R. C.: Atmospheric NO₂: in situ laser-induced fluorescence detection at parts per trillion mixing ratios, *Anal. Chem.*, 72, 528–539, <https://doi.org/10.1021/ac9908905>, <https://doi.org/10.1021/ac9908905>, 2000.
- 830 Tzortziou, M., Herman, J. R., Cede, A., Loughner, C. P., Abuhassan, N., and Naik, S.: Spatial and temporal variability of ozone and nitrogen dioxide over a major urban estuarine ecosystem, *J. Atmos. Chem.*, 72, 287–309, <https://doi.org/10.1007/s10874-013-9255-8>, <https://doi.org/10.1007/s10874-013-9255-8>, 2015.
- Tzortziou, M., Parker, O., Lamb, B., Herman, J. R., Lamsal, L., Stauffer, R., and Abuhassan, N.: Atmospheric trace gas (NO₂ and O₃) variability in South Korean coastal waters, and implications for remote sensing of coastal ocean color dynamics, *Remote Sensing*, 10, 1587, <https://doi.org/10.3390/rs10101587>, <https://www.mdpi.com/2072-4292/10/10/1587>, 2018.
- 835 Valin, L. C., Russell, A. R., and Cohen, R. C.: Variations of OH radical in an urban plume inferred from NO₂ column measurements, *Geophys. Res. Lett.*, 40, 1856–1860, <https://doi.org/10.1002/grl.50267>, <https://agupubs.onlinelibrary.wiley.com/doi/abs/10.1002/grl.50267>, 2013.
- van der A, R. J., Eskes, H. J., Boersma, K. F., Noije, T. P. C. v., Roozendael, M. V., Smedt, I. D., Peters, D. H. M. U., and Meijer, E. W.: Trends, seasonal variability and dominant NO_x source derived from a ten year record of NO₂ measured from space, *J. Geophys. Res. Atmos.*, 113, D04 302, <https://doi.org/10.1029/2007JD009021>, <https://agupubs.onlinelibrary.wiley.com/doi/abs/10.1029/2007JD009021>, 2008.
- 840 van Noije, T. P. C., Eskes, H. J., Dentener, F. J., Stevenson, D. S., Ellingsen, K., Schultz, M. G., Wild, O., Amann, M., Atherton, C. S., Bergmann, D. J., Bey, I., Boersma, K. F., Butler, T., Cofala, J., Drevet, J., Fiore, A. M., Gauss, M., Hauglustaine, D. A., Horowitz, L. W., Isaksen, I. S. A., Krol, M. C., Lamarque, J.-F., Lawrence, M. G., Martin, R. V., Montanaro, V., Müller, J.-F., Pitari, G., Prather, M. J., Pyle, J. A., Richter, A., Rodriguez, J. M., Savage, N. H., Strahan, S. E., Sudo, K., Szopa, S., and Roozendael, M. v.: Multi-model ensemble simulations of tropospheric NO₂ compared with GOME retrievals for the year 2000, *Atmos. Chem. Phys.*, 6, 2943–2979, <https://doi.org/https://doi.org/10.5194/acp-6-2943-2006>, <https://www.atmos-chem-phys.net/6/2943/2006/>, 2006.
- 845 Vandaele, A. C., Hermans, C., Simon, P. C., Carleer, M., Colin, R., Fally, S., Mérienne, M. F., Jenouvrier, A., and Coquart, B.: Measurements of the NO₂ absorption cross-section from 42 000 cm⁻¹ to 10 000 cm⁻¹ (238–1000 nm) at 220 K and 294 K, *J. Quant. Spectrosc. Ra.*, 59, 171–184, [https://doi.org/10.1016/S0022-4073\(97\)00168-4](https://doi.org/10.1016/S0022-4073(97)00168-4), <http://www.sciencedirect.com/science/article/pii/S0022407397001684>, 1998.
- 850 Vasilkov, A., Qin, W., Krotkov, N., Lamsal, L., Spurr, R., Haffner, D., Joiner, J., Yang, E.-S., and Marchenko, S.: Accounting for the effects of surface BRDF on satellite cloud and trace-gas retrievals: a new approach based on geometry-dependent Lambertian equivalent reflectivity applied to OMI algorithms, *Atmos. Meas. Tech.*, 10, 333–349, <https://doi.org/10.5194/amt-10-333-2017>, <https://www.atmos-meas-tech.net/10/333/2017/>, 2017.
- Vasilkov, A., Yang, E.-S., Marchenko, S., Qin, W., Lamsal, L., Joiner, J., Krotkov, N., Haffner, D., Bhartia, P. K., and Spurr, R.: A cloud algorithm based on the O₂-O₂ 477 nm absorption band featuring an advanced spectral fitting method and the use of surface geometry-dependent Lambertian-equivalent reflectivity, *Atmos. Meas. Tech.*, 11, 4093–4107, <https://doi.org/10.5194/amt-11-4093-2018>, <https://www.atmos-meas-tech.net/11/4093/2018/>, 2018.
- 855 Veeffkind, J. P., Haan, J. F. d., Sneep, M., and Levelt, P. F.: Improvements to the OMI O₂-O₂ operational cloud algorithm and comparisons with ground-based radar-lidar observations, *Atmos. Meas. Tech.*, 9, 6035–6049, <https://doi.org/https://doi.org/10.5194/amt-9-6035-2016>, <https://www.atmos-meas-tech.net/9/6035/2016/>, 2016.



- 860 Vinken, G. C. M., Boersma, K. F., van Donkelaar, A., and Zhang, L.: Constraints on ship NO_x emissions in Europe using GEOS-Chem and OMI satellite NO_2 observations, *Atmos. Chem. Phys.*, 14, 1353–1369, <https://doi.org/https://doi.org/10.5194/acp-14-1353-2014>, <https://www.atmos-chem-phys.net/14/1353/2014/>, 2014.
- Vlemmix, T., PETERS, A. J. M., Stammes, P., Wang, P., and Levelt, P. F.: Retrieval of tropospheric NO_2 using the MAX-DOAS method combined with relative intensity measurements for aerosol correction, *Atmos. Meas. Tech.*, 3, 1287–1305, <https://doi.org/10.5194/amt-3-1287-2010>, <https://www.atmos-meas-tech.net/3/1287/2010/>, 2010.
- 865 Wang, S. W., Zhang, Q., Streets, D. G., He, K. B., Martin, R. V., Lamsal, L. N., Chen, D., Lei, Y., and Lu, Z.: Growth in NO_x emissions from power plants in China: bottom-up estimates and satellite observations, *Atmos. Chem. Phys.*, 12, 4429–4447, <https://doi.org/https://doi.org/10.5194/acp-12-4429-2012>, <https://www.atmos-chem-phys.net/12/4429/2012/>, 2012.
- WHO: Review of evidence on health aspects of air pollution REVIHAAP Project, Tech. rep., p. 302, World Health Organization, 870 Copenhagen, Denmark, http://www.euro.who.int/__data/assets/pdf_file/0004/193108/REVIHAAP-Final-technical-report-final-version.pdf?ua=1, 2013.
- Wild, R. J., Edwards, P. M., Dubé, W. P., Baumann, K., Edgerton, E. S., Quinn, P. K., Roberts, J. M., Rollins, A. W., Veres, P. R., Warneke, C., Williams, E. J., Yuan, B., and Brown, S. S.: A measurement of total reactive nitrogen, NO_y , together with NO_2 , NO , and O_3 via cavity ring-down spectroscopy, *Environ. Sci. Technol.*, 48, 9609–9615, <https://doi.org/10.1021/es501896w>, <https://doi.org/10.1021/es501896w>, 875 2014.
- Wong, D. C., Pleim, J., Mathur, R., Binkowski, F., Otte, T., Gilliam, R., Pouliot, G., Xiu, A., Young, J. O., and Kang, D.: WRF-CMAQ two-way coupled system with aerosol feedback: software development and preliminary results, *Geoscientific Model Development*, 5, 299–312, <https://doi.org/10.5194/gmd-5-299-2012>, <https://www.geosci-model-dev.net/5/299/2012/>, 2012.
- Yarwood, G., Rao, S., Yocke, M., and Whitten, G.: Updates to the Carbon Bond Chemical Mechanism: CB05. RT-0400675, vol. 8, U.S. 880 Environmental Protection Agency, Washington, District of Columbia, USA, 2005.
- Zhao, C. and Wang, Y.: Assimilated inversion of NO_x emissions over east Asia using OMI NO_2 column measurements, *Geophys. Res. Lett.*, 36, L06 805, <https://doi.org/10.1029/2008GL037123>, <https://agupubs.onlinelibrary.wiley.com/doi/abs/10.1029/2008GL037123>, 2009.
- Zhou, D. K., Larar, A. M., Liu, X., Smith, W. L., Strow, L. L., Yang, P., Schlüssel, P., and Calbet, X.: Global Land Surface Emissivity Retrieved From Satellite Ultraspectral IR Measurements, *IEEE Trans. Geosci. Remote Sens.*, 49, 1277–1290, 885 <https://doi.org/10.1109/TGRS.2010.2051036>, 2011.

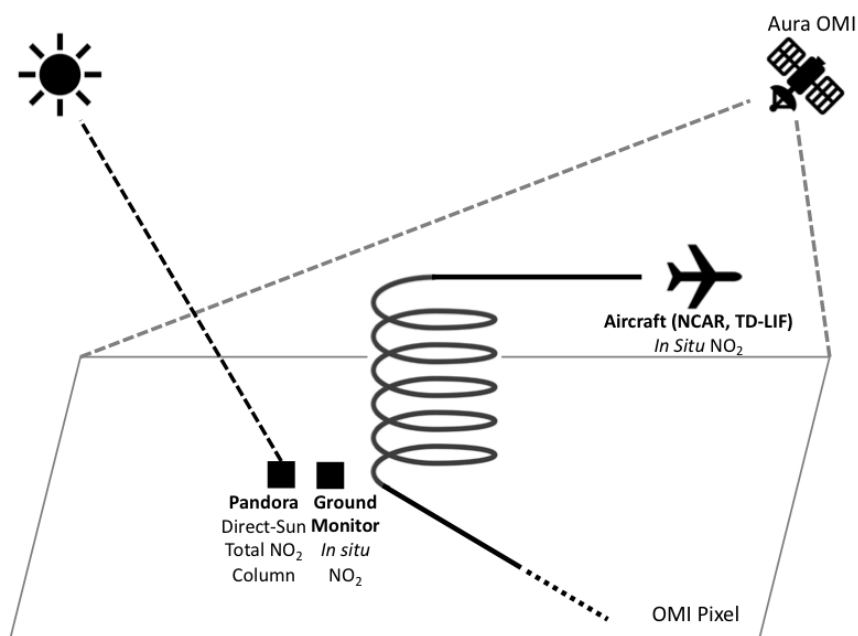


Figure 1. Conceptual illustration of NO_2 observations during the DISCOVER-AQ and KORUS-AQ field campaigns. The instruments used include ground-based monitors measuring in situ NO_2 volume mixing ratios, Pandora making direct-sun measurements to retrieve the total column NO_2 , airborne instruments measuring in situ NO_2 profiles, and the Ozone Monitoring Instrument (OMI) aboard the Aura spacecraft reporting total and tropospheric columns NO_2 .

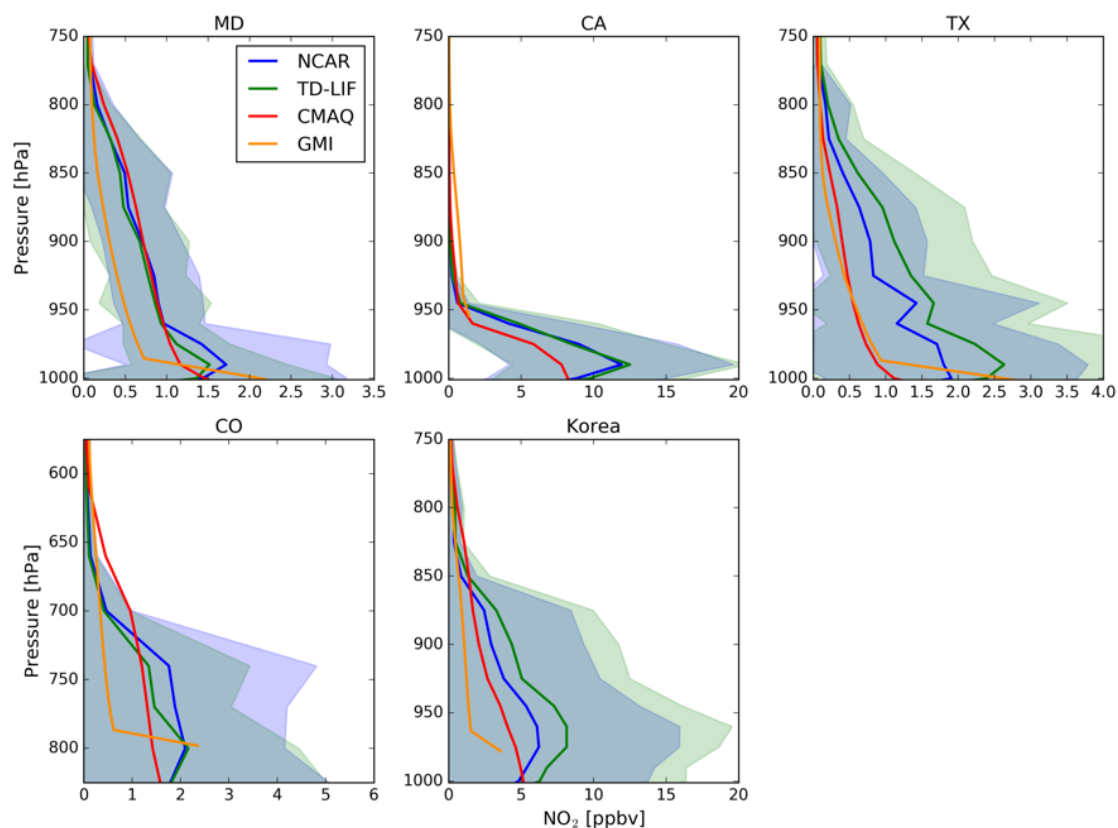


Figure 2. Mean early afternoon NO₂ profiles, both observed and modeled, for the DISCOVER-AQ and KORUS-AQ campaigns. Colored lines represent the average for airborne in situ profiles from NCAR (blue) and TD-LIF (green) instruments compared with simulated profiles from the GMI global model (orange) and the CMAQ (DISCOVER-AQ) or WRF-Chem (KORUS-AQ) regional models (red). The standard deviations of airborne profiles are indicated as shaded areas for NCAR (lavender) and TD-LIF (green) instruments. The blue-gray color represents the overlap of the two.

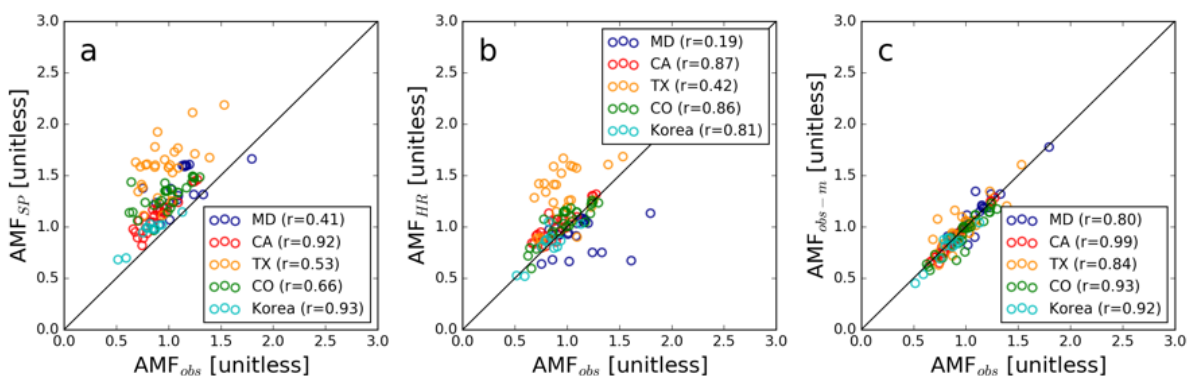


Figure 3. Comparison of AMFs calculated using observed NO₂ profiles (AMF_{obs}) with tropospheric AMFs in the OMI standard product (AMF_{SP}, 3a), and those calculated using NO₂ profiles from high-resolution model simulations (AMF_{HR}, 3b). The right panel (3c) compares tropospheric AMFs using daily versus campaign-average profiles (AMF_{obs-m}). The symbols are color-coded by campaign locations.

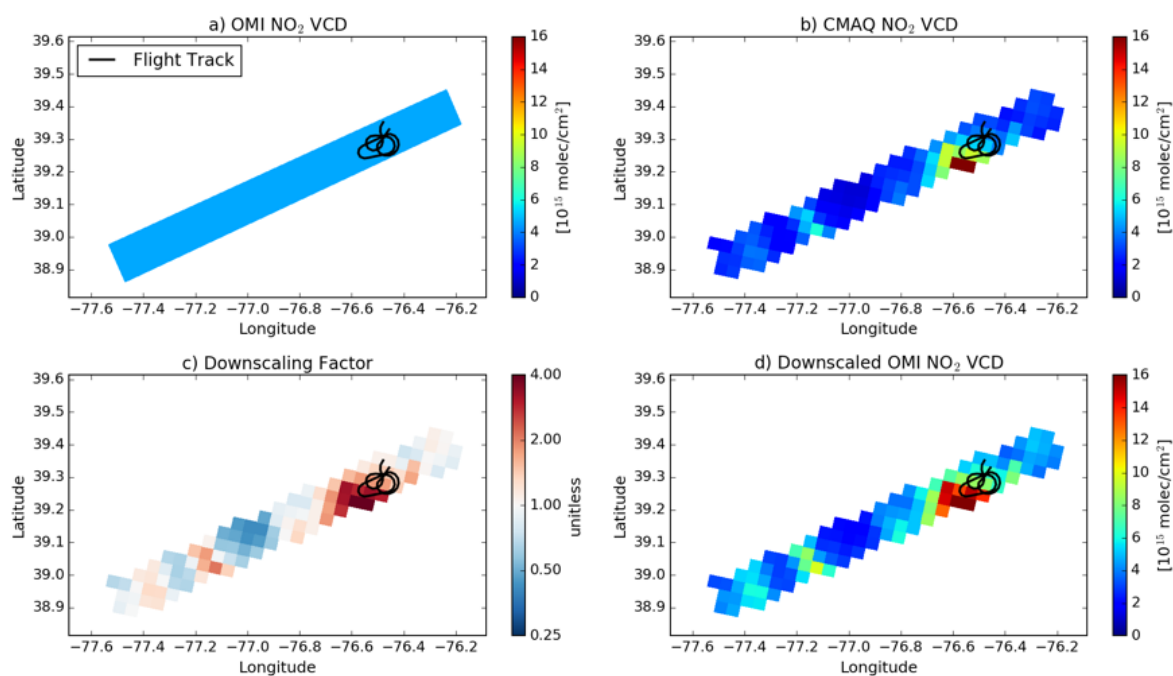


Figure 4. An illustration of downscaled OMI NO₂ for an OMI pixel over MD from orbit 37024 on July 1, 2011. Shown are the original OMI tropospheric NO₂ VCD (a), coincidentally sampled CMAQ NO₂ VCD at a spatial resolution of 4×4 km² (b), the spatial weighting kernel (c), and downscaled OMI tropospheric NO₂ VCD (d). These pixels coincide with an airborne in situ NO₂ profile sampled during the DISCOVER-AQ Maryland campaign, and the flight route is marked with a black line.

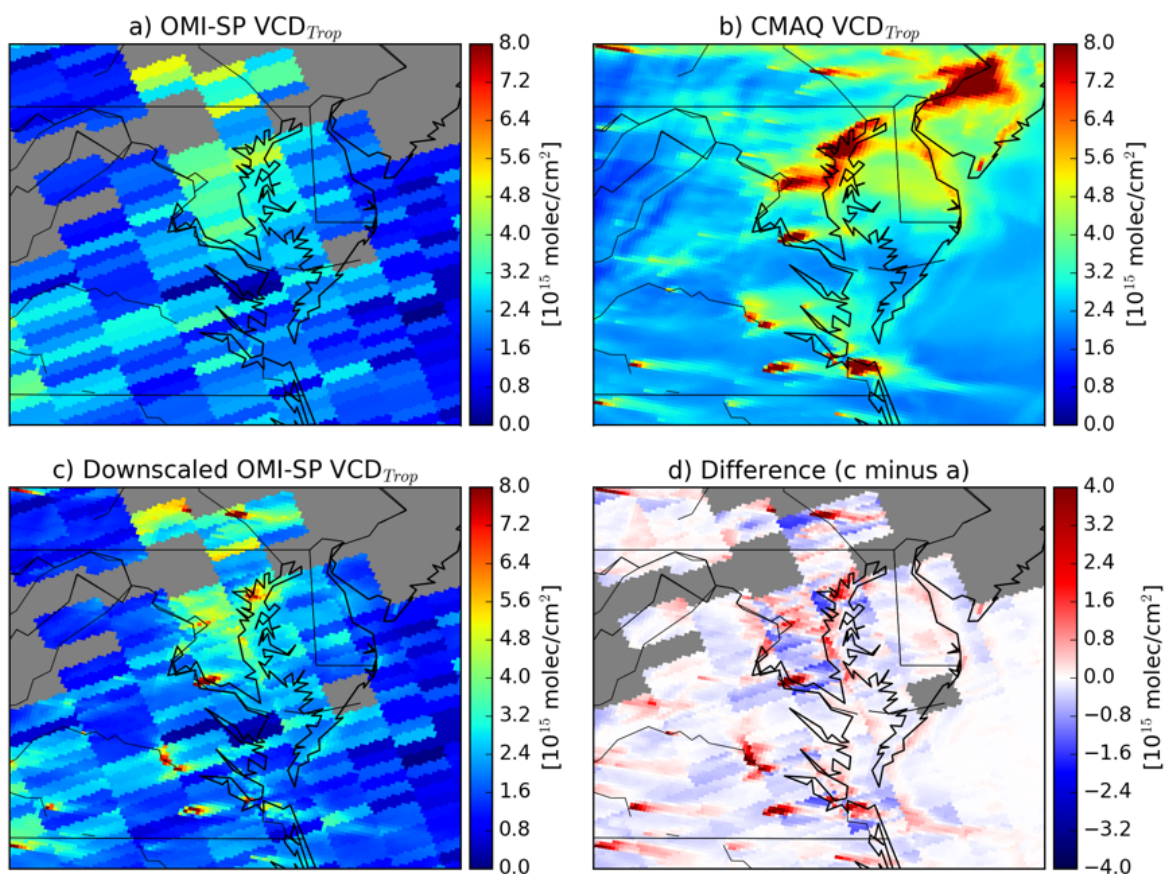


Figure 5. Tropospheric NO₂ VCD maps from (a) OMI SP, (b) CMAQ, and (c) downscaled OMI on July 29, 2011. The panel (d) shows the difference between downscaled and standard tropospheric NO₂ VCD data (c minus a). The gray areas represent pixels with effective cloud fraction > 0.3.

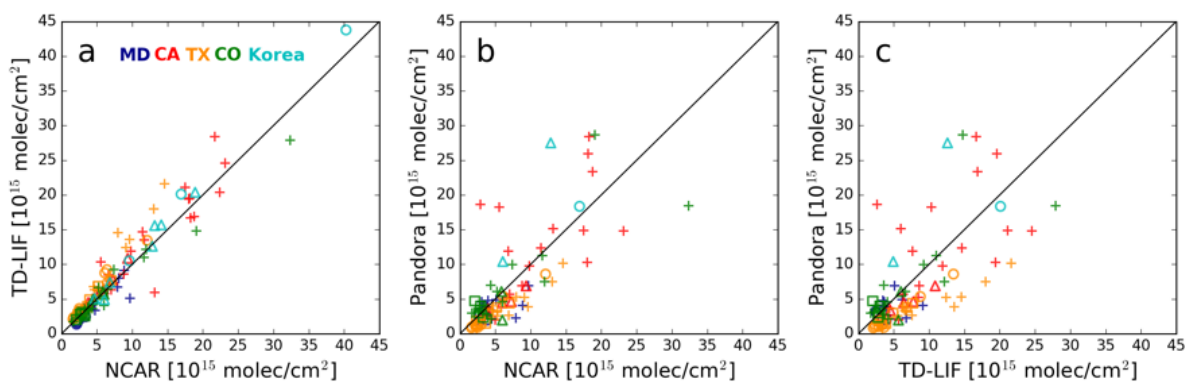


Figure 6. Comparison of NO_2 tropospheric columns derived from NCAR, TD-LIF, and Pandora instruments. Different colors represent the campaign location, and the symbols represent the type of surface monitors (open circle: photolytic converter, plus: molybdenum converter, triangle: CAPS, and square: CRDS).

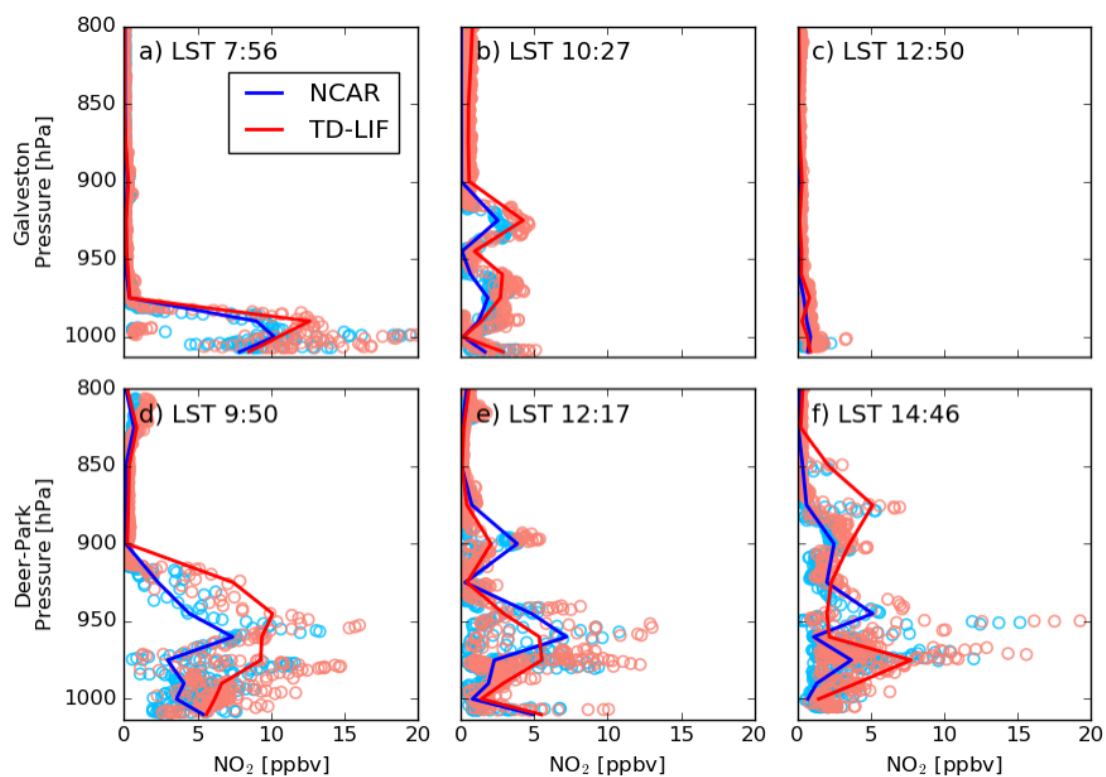


Figure 7. Vertical distribution of NO_2 mixing ratios at different local solar time (LST) over Galveston (top) and Deer-Park (bottom) in TX measured by the NCAR (light blue) and TD-LIF (orange) instruments. The circles in lighter colors represent 1-second measurements, and the solid lines show the mean values for NCAR (blue) and TD-LIF (red).

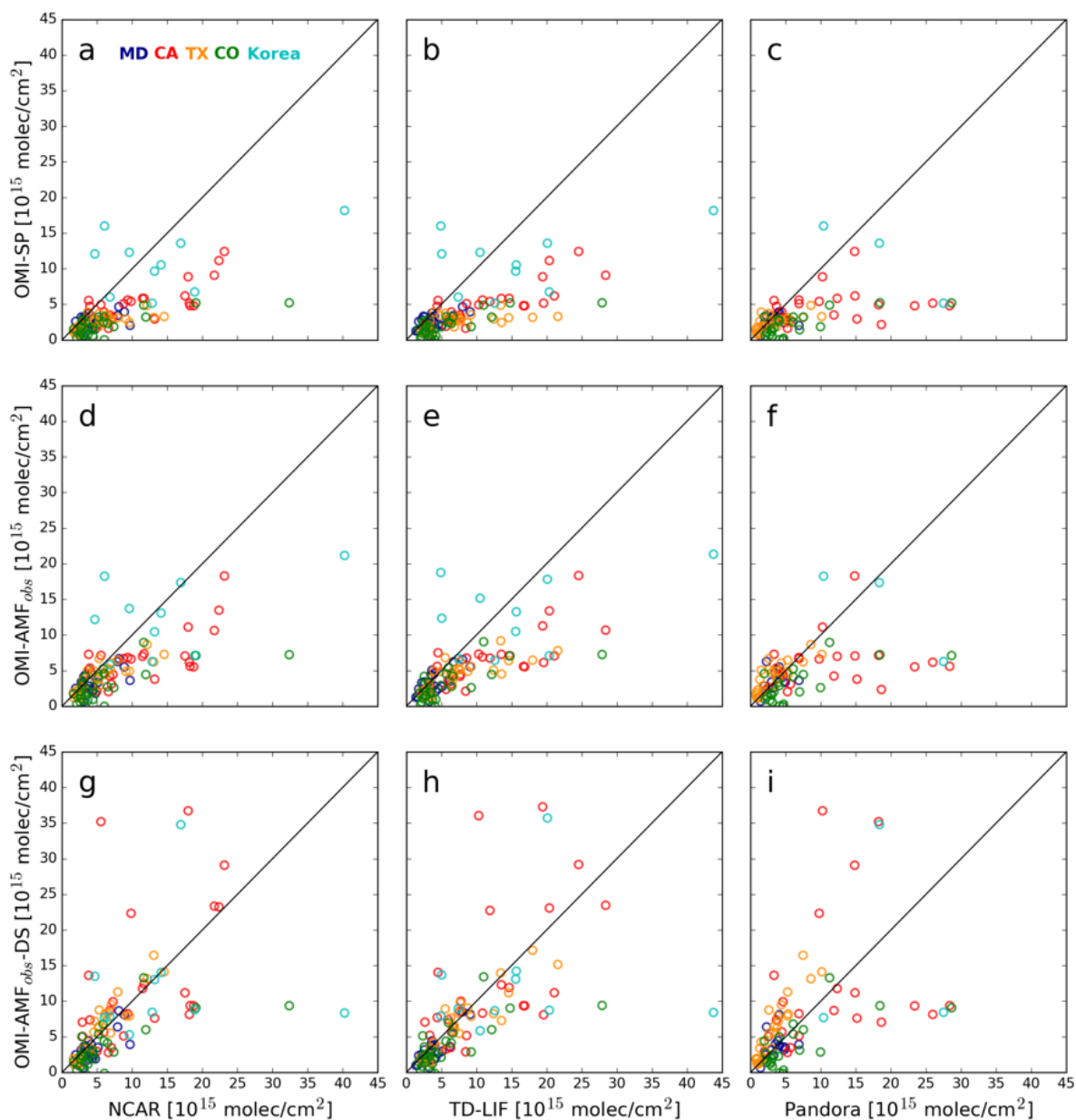


Figure 8. Comparison of tropospheric NO_2 columns from OMI with the data from NCAR (a, d, g), TD-LIF (b, e, h), and Pandora (c, f, i) instruments. OMI retrievals are performed using the default GMI (a-c), observed NO_2 profiles (d-i), or are downscaled (g, h, i) using a high-resolution (CMAQ/WRF-Chem) model simulations. Different colors represent the campaign locations.

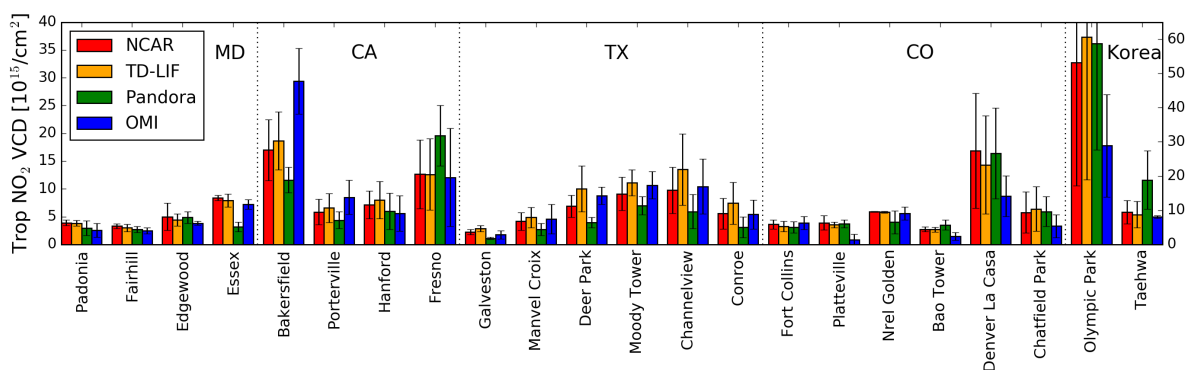


Figure 9. Site mean tropospheric NO₂ VCDs calculated from NCAR (red), TD-LIF (orange), Pandora (green), and OMI (blue) instruments. The OMI data are derived using observed NO₂ profiles and downscaled using high-resolution model simulations. The vertical bars represent the standard deviations. A different y scale (on right, 0-65 × 10¹⁵ molec./cm²) is used for Korea.



Table 1. Campaign locations and time periods.

Campaign	Location	Time period	Flight days
DISCOVER-AQ	Baltimore, Maryland	June–July 2011	14
DISCOVER-AQ	San Joaquin Valley, California	January–February 2013	11
DISCOVER-AQ	Houston, Texas	September 2013	10
DISCOVER-AQ	Denver–Ft. Collins, Colorado	July–August 2014	15
KORUS-AQ	Republic of Korea (South Korea)	May–June 2016	22



Table 2. Summary of ground supersites during DISCOVER-AQ and KORUS-AQ campaigns with ground based NO₂ measurements. The symbol N represents the sample size for aircraft and Pandora (in parentheses) measurements that are collocated with OMI observations. Surface NO₂ monitors include NO_x analyzers with molybdenum converters (MC), NO_x analyzers with photolytic converters (PC), Cavity Attenuated Phase Shift (CAPS), and Cavity Ring-Down Spectroscopy (CRDS).

Campaign	Site	Latitude/Longitude	Elevation (m)	N	Ground monitor type
MD	Padonia	39.46°N, 76.63°W	120	6 (4)	PC
	Fairhill	39.7°N, 76.86°W	109	3	PC
	Edgewood	39.4°N, 76.47°W	9	6 (5)	PC
	Essex	39.31°N, 76.3°W	13	3 (2)	MC
	Chesapeake*	39.16°N, 76.34°W**	-	3 (0)	-
CA	Bakersfield	35.33°N, 119.0°W	117	5 (3)	MC
	Porterville	36.03°N, 119.06°W	141	5	CAPS
	Hanford	36.32°N, 119.64°W	80	7 (6)	MC
	Fresno	36.79°N, 119.77°W	97	8	MC
TX	Galveston	29.25°N, 94.86°W	0	7	PC
	Manvel Croix	29.52°N, 95.39°W	18	6	CRDS
	Deer Park	29.67°N, 95.13°W	6	4	MC
	Moody Tower	29.72°N, 95.34°W	64	4 (2)	PC
	Channelview	29.80°N, 95.13°W	6	4	MC
	Conroe	30.35°N, 95.43°W	67	3	MC
CO	Fort Collins	40.59°N, 105.14°W	1577	3 (2)	MC
	Platteville	40.18°N, 104.73°W	1522.5	5 (4)	MC
	NREL-Golden	39.74°N, 105.18°W	1846	4 (2)	CAPS
	Bao Tower	40.04°N, 105.01°W	1590	4	CRDS
	Denver La Casa	39.78°N, 105.01°W	1602	5 (4)	MC
	Chatfield Park	39.53°N, 105.07°W	1675	5	MC
Korea	Olympic Park	37.52°N, 127.124°E	26	4 (3)	PC
	Taehwa	37.31°N, 127.311°E	160	7 (2)	CAPS

*Only aircraft spirals were performed over this site.

**The coordinate is approximate.



Table 3. Comparison between NCAR, TD-LIF, and Pandora NO₂ observations.

Campaign	NCAR vs. TD-LIF Mean Diff. (%)		NCAR vs. Pandora Mean Diff. (%)		TD-LIF vs. Pandora Mean Diff. (%)	
	(TD-LIF – NCAR)	r	(Pandora – NCAR)	r	(Pandora – TD-LIF)	r
MD	-9.6	0.87	-24.5	0.42	-18.3	0.18
CA	7.2	0.93	11.1	0.65	4.8	0.58
TX	31.9	0.97	-39.1	0.94	-53.9	0.93
CO	-6.6	0.99	-2.8	0.81	4.2	0.78
Korea	11.6	0.99	20.3	0.95	7.5	0.94

Table A1. Model options for each simulation. Note that all model options listed are for the domain used for the analysis.

	MD	CA	TX	CO	Korea
<i>Dates</i>	5/24/2011–8/1/2011	1/10/2013–2/28/2013	8/18/2013–10/1/2013	7/9/2014–08/20/2014	5/1/2016–5/31/2016
WRF Model Options					
<i>Version</i>	3.3	3.8	3.6.1	3.8.1	3.6.1
<i>Model Top</i>	100 hPa	50 hPa	50 hPa	50 hPa	50 hPa
<i>Spatial Resolution</i>	4 km	4 km	4 km	4 km	4 km
<i>Vertical Levels</i>	34	35	45	37	52
<i>Radiation</i>	LW: RRTM SW: Goddard	LW: RRTMG SW: RRTMG	LW: RRTM SW: Goddard	LW: RRTMG SW: RRTMG	LW: RRTM SW: Goddard
<i>Land Surface Model</i>	Noah Land Surface Model (Tewari et al., 2004)	Pleim-Xiu (Pleim and Xiu, 2003)	Pleim-Xiu (Pleim and Xiu, 2003)	Unified Noah Land Surface Model	Unified Noah Land Surface Model
<i>Boundary Layer Meteor. Init. and Bound. Cond.</i>	YSU (Hong et al., 2006) 12 km NAM	ACM2 (Pleim, 2007) 12 km NAM	ACM2 (Pleim, 2007) 12 km NAM	YSU (Hong et al., 2006) NCAR ECMWF	MJY scheme 0.25 degree GFS
CMAQ Model Options					
<i>Version</i>	5.0	5.2	5.0.2	5.2 beta	3.6.1 (modified)
<i>Coupled?</i>	No	Yes	No	No	Yes
<i>Chemical Mechanism</i>	Carbon Bond (CB05) (Yarwood et al., 2005)	Carbon Bond (CB06, e51)	Carbon Bond (CB05) (Yarwood et al., 2005)	Carbon Bond (CB06, r3)	Reduced hydrocarbon (Pfister et al., 2014)
<i>Aerosol</i>	AE5	AERO6	AE5	AERO6	MOSAIC 4 bin
<i>Chem. Init. and Bound. Cond.</i>	12 km CMAQ v5.0 simulation Described in Loughner et al. (2014)	12-km CMAQ v5.2 simulation 4km (based off the 2011 NEI with year-specific updates to EGU point sources (CEMs data), fires and mobile emissions (MOBILE6))	MOZART (Outer domain) main)	RAQMS (Outer domain)	24 km MACC for chemistry
<i>Emissions</i>			2012 TCEQ anthropogenic emissions Bio-genic Emission Inventory System (BEIS) calculated within CMAQ	Described in report: https://www.colorado.gov/airquality/tech_doc_repository.aspx?action=open&file=FRAPPE-NCAR_Final_Report_July2017.pdf	Described in Goldberg et al. (2019) and Saide et al. (in preparation)

LW: Long Wave, SW: Short Wave, RRTM: Rapid Radiative Transfer Model, RRTMG: Rapid Radiative Transfer Model for General Circulation Models, AE5: Aerosols with aqueous extensions version 5, MOZART: Model for Ozone and Related chemical Tracers, RAQMS: Real Time Air Quality Monitoring System, MACC: Monitoring Atmospheric Composition and Climate



Table A2. Summary of NO₂ comparison between OMI Standard Product (OMI_{SP}) and NCAR, TD-LIF, and Pandora observations. The mean difference is calculated as OMI minus observations.

Campaign	NCAR vs. OMI _{SP}		TD-LIF vs. OMI _{SP}		Pandora vs. OMI _{SP}	
	Mean Diff. (%)	r	Mean Diff. (%)	r	Mean Diff. (%)	r
MD	-40.7	0.39	-34.4	0.54	-21.8	0.21
CA	-53.8	0.77	-56.9	0.81	-58.5	0.24
TX	-54.9	0.65	-65.8	0.56	-26.9	0.65
CO	-67.5	0.73	-65.2	0.75	-68.2	0.72
Korea	-41.9	0.87	-47.9	0.87	-60.1	0.8



Table A3. Same as A2, but for OMI using AMF_{obs} (OMI_{obs}).

Campaign	NCAR vs. OMI_{obs}		TD-LIF vs. OMI_{obs}		Pandora vs. OMI_{obs}	
	Mean Diff. (%)	r	Mean Diff. (%)	r	Mean Diff. (%)	r
MD	-23.7	0.61	-17.6	0.7	2.4	0.3
CA	-42.4	0.73	-45.8	0.75	-47.9	0.2
TX	-25.5	0.82	-41.3	0.76	21.6	0.81
CO	-54.2	0.7	-50.5	0.71	-55.2	0.69
Korea	-33.9	0.87	-39.2	0.86	-53.3	0.79



Table A4. Same as A2, but for OMI_{obs} with downscaling (OMI_{DS}).

Campaign	NCAR vs. OMI_{DS}		TD-LIF vs. OMI_{DS}		Pandora vs. OMI_{DS}	
	Mean Diff. (%)	r	Mean Diff. (%)	r	Mean Diff. (%)	r
MD	-24.1	0.75	-18.0	0.85	0.8	0.31
CA	14.2	0.47	7.6	0.56	4.6	0.22
TX	9.5	0.94	-13.8	0.91	78.3	0.93
CO	-42.4	0.7	-37.7	0.71	-42.4	0.67
Korea	-32.8	0.73	-38.4	0.73	-52.1	0.48